J. Mex. Chem. Soc. **2023**, *67*(4)
Special Issue
©2023, Sociedad Química de México
ISSN-e 2594-0317

Microstructures of Binary Oxides with an Inverse Opal Structure Used as Photoelectrodes for Water Splitting

---

Manuel Humberto Ríos-Domínguez[1], Bernardo A. Frontana-Uribe[1,2] *

[1]Centro Conjunto de Investigación en Química Sustentable UAEMéx-UNAM, Km 14.5 Carretera Toluca-Atlacomulco, Toluca 50200, México.
[2]Universidad Nacional Autónoma de México, Instituto de Química, Ciudad Universitaria, México City 04510, México.

***Corresponding author:** Bernardo A. Frontana-Uribe, email: bafrontu@unam.mx

Received March 10th, 2023; Accepted August 17th, 2023.

DOI: http://dx.doi.org/10.29356/jmcs.v67i4.1998

This work is in honor of all the emeritus professors of SNI (México) in the electrochemistry area until 2022, Elsa Arce, Joan Genescá, Ignacio González, Jorge Ibañez, Yunni Meas and Omar Solorza, who had founded our modern vision of electrochemistry. Thanks for your pioneering works!!

Abstract. Recently, the weather has experienced changes and these have affected our life style. Fossil fuels used by the human have contributed to climate change and today it is impossible to modify. Researchers have studied different kind of fuels that could use daily. Currently, hydrogen, from water splitting, is the best way to substitute the fossil fuels because water is present around the World. In photoelectrochemistry, the electrodes have a great importance. Behaviour of each semiconductor as TiO_2, Fe_2O_3, NiO, CuO, NiS, ZnO, Cu_2O, etc., give us individual efficiency respect to solar light. Also, the semiconductor chosen, type of crystallinity and superficial area are important points for achieve high in efficiency. This review shows that inverse opal has a greater contact compared to rod, cauliflower, nanotubes, etc. Different ways to deposit the polystyrene allows us gain more contact area and better photoelectrode efficiency. The main routes used to obtain binary oxides deposits, as electrophoretic, spin coating, vertical submersion, etc., help us to control polystyrene arrangement and obtain a uniform template. These techniques are discussed along this contribution.
Keywords: Inverse opal; water splitting; template; hematite; titanium oxide; zinc oxide; copper (I) oxide; nickel sulfide; nickel oxide; photoelectrode.

Resumen. Recientemente, el clima ha experimentado cambios que han afectado a nuestro estilo de vida. Los combustibles fósiles utilizados por el ser humano han contribuido al cambio climático y hoy es imposible modificarlo. Los investigadores estudian diferentes tipos de combustibles que podrían utilizarse diaria y actualmente, el hidrógeno, a partir de la ruptura de la molécula de agua, es la mejor manera de sustituir los combustibles fósiles porque el agua está presente en todo el mundo. En fotoelectroquímica, los electrodos tienen una gran importancia. El comportamiento de cada semiconductor como TiO_2, Fe_2O_3, NiO, CuO, NiS, ZnO, Cu_2O, etc., tiene cada uno una eficiencia individual respecto a la luz solar que reciben. Además, del semiconductor elegido, el tipo de cristalinidad y el área superficial de este son puntos determinantes para alcanzar un alto grado de eficiencia. La presente revisión muestra que el ópalo inverso tiene un mayor contacto y eficiencia en comparación con las varillas, la coliflor, los nanotubos, etc. Diferentes formas de depositar el poliestireno como molde nos permiten obtener mayor área de contacto y mejor eficiencia del fotoelectrodo semiconductor. Las principales vías utilizadas para obtener depósitos de óxidos binarios, como electroforesis vertical, etc., nos ayudan a controlar la disposición del poliestireno y obtener una capa uniforme. Estas técnicas se discuten a lo largo de esta contribución.

Palabras clave: Ópalo inverso; ruptura de agua; molde; hematita; dióxido de titanio; óxido de zinc; óxido de cobre (I); sulfuro de níquel; óxido de níquel; fotoelectrodo.

Abbreviations

Air Mass	(AM)
Atomic Layer Deposit	(ALD)
Bandgap Energy	(E_g)
Body Centered Cubic	(BCC)
Direct Current	(DC)
Electrophoretic Deposition	(EPD)
Face-Centered Cubic	(FCC)
Fluorine dopedTin Oxide	(FTO)
Hexagonal Close Packed	(hcp)
Highest Occupied Molecular Orbital	(HOMO)
Hydrogen Evolution Reaction	(HER)
Hydrogen Evolution Reaction	(HER)
Indium Tin Oxide	(ITO)
Interstitial Oxygen	(O_i)
Interstitial Zinc	(Zn_i)
Lowest Unoccupied Molecular Orbital	(LUMO)
Normal Hydrogen Electrode	(NHE)
Oxygen Evolution Reaction	(OER)
Oxygen Vacancies	(V_O)
Photoelectrochemical	(PEC)
Polyethylene Terephthalate	(PET)
Polymethyl methacrylate	(PMMA)
Polystryrene	(PS)
Potential of the Conduction Band	(E_{CB})
Reversible Hydrogen Electrode	(RHE)
Saturated Calomel Electrode	(SCE)
Scanning Electron Microscopy	(SEM)
Solar to Hydrogen conversion efficiency	(STH)
Specific Capacitance	(C_m)
Standard Hydrogen Electrode	(SHE)
Transmission Electron Microscopy	(TEM)
Transparent Conductive Oxide	(TCO)

Introduction

Today 80 % of the global energy demand is covered by fossil fuels [1]. This gives rise to shortages of these and the increase in environmental problems. That is why it is important to develop clean, cheap, renewable and sustainable energy resources. The breakdown of the water molecule to produce hydrogen (hydrogen evolution reaction, HER) is a promising way to solve these problems. Additionally, the oxygen evolution reaction (OER) is used in environmental remediation applications by generating useful species for pollutant degradation [2]. Of these two half-reactions, the OER is the one that requires the greatest energy demand by applying a large overpotential for its realization [3]. For environmental issues, it has been found that the combustion of hydrogen to generate energy produces water with many advantages, without hazardous residues whose only residue is water and without causing the increase of CO_2 [4]. In addition, it has higher energy per unit mass (Table I), it can be easily stored, obtained from water, and directly converted into thermal, mechanical, and electrical energy [5].

Table 1. Heat of combustion of different fuels [5].

Fuel	**Energy ($kcal\ gr^{-1}$)**
hydrogen	34.0
petroleum	10.3 – 8.4
paraffin	10.3 – 9.8
graphite (coal)	7.8
castor oil	9.4
wood	4.2

It has been determined that the available solar energy striking the earth's surface at any time is equal to *ca.* 130 million of MW. To cover the global energy demand, three main points must be met: conversion, storage and distribution of solar energy [6]. For this reason, the conversion of solar energy into other forms of energy represents a need and an interest today, within which solar water- splitting represents a promising option [7]. The production processes of hydrogen depend on the raw materials used. In Fig. 1 we see its origin from fossil fuels and renewable resources. For renewable resources, the breakdown of the water molecule is divided into electrolysis, thermolysis and photolysis [8]. Photolysis can be compared to photosynthesis where plants convert photon energy into chemical energy such as sugars and oxygen (Fig. 2) [9]. In natural photosynthesis, plants use sunlight and, from water and carbon dioxide are produced oxygen and carbohydrates. They collect light energy through an assembly of light-harvesting chlorophylls and pump electrons to a higher electronic state inside a reaction center. Photosystems are connected in series with an electron transfer chain. This electronic transfer (charge-separation processes) included type I and II reaction centers. This process is known as the Z scheme. The artificial photosystems reactions have three reactions: light-harvesting, charge generation and separation, with catalytic reaction processes [10]. Photocatalysis are reactions that use light and a semiconductor. When the semiconductor is exposed to light is generated an electron/hole pair. Exits two types of photocatalytic reactions: Homogeneous photocatalysis: semiconductor and reactant are in the same phase, and Heterogeneous photocatalysis: semiconductor and reactant are in different phases [11]. The processes involved in photocatalytic reactions have some notable points: the photon absorption, which generates an exciton, and the efficiency of this process depends on the electronic structure of the material irradiated. Different structure reveals different visible-light response, and the overall reaction is associated with defects on the surface and crystallinity. The geometric area, where the photon is striking, limits the quantity of electron-hole pairs on the semiconductor, and it depends on the thickness of the material and the wavelength used. The exciton binding energy dictates the energy required to ionize an exciton from the lowest energy state, and it is associated with the carrier lifetime is a crucial parameter to classify the effectiveness of photocatalysts. The generated free carriers are transferred to redox-active sites on the catalyst surface. This mobility requires carrier diffusion and transport through the bulk of the semiconductor. Electrocatalytic activity is generated when the accumulation of electrons/holes at redox-active sites happens, and the electroactive species reach these regions. Mass transfer influences overall efficiency by creating a concentration gradient, while its consumption leads to the depletion of reactant concentration at the surface. The mass transport flux is affected by the size of the species, the solution viscosity, the diffusion coefficient, and species activity. Additionally, overpotential causes an additional loss of overall efficiency [12] and is the difference between the quasi-Fermi level of holes and the electrochemical potential of the solution [13]. The semiconductor electrode under lightning must be stable. This stability depends on preparation, dopant, pretreatment, dissolution, and lighting conditions [14]. A fundamental factor to calculate in photocatalysis is the solar-to-Hydrogen (STH) energy efficiency. It is the energy conversion efficiency from input solar energy to produced chemical energy.

$$STH(\%) = \frac{output\ energy\ of\ hydrogen\ evolved}{energy\ of\ incident\ solar\ light} x100 = \frac{(mmol\ H_2 s^{-1})\ x\ 237\ (kJmol^{-1})}{p_{in}\ (MW\ cms^{-2}) x\ area\ (cm^2)} x100$$

The equation shows us how the chemical energy is produced at the rate of H_2 multiplied by the charge in Gibbs free energy (25 °C). The solar energy input is the energy flux of sunlight (p_{in}) multiplied by the effective area of incident light on the semiconductor (photoelectrode). It is important to highlight the importance to using an adequate photoelectroactive area. The light sources more used in photocatalysis are xenon (Xe) lamps, mercury (Hg) lamps, and light-emitting diodes (LED). Various incident photon fluxes produce different photocatalytic performances even for the same photocatalyst. Using lamps does not allow comparing the results with the authentic sunlight. Each light source has its own working lifespan, and the experiments have to be measured when is sure the stability of the light source (each lamp has itself stability time). Other experimental errors with light sources are when the reaction use different material of the reactor, the distance between the light and the reactor, and the irradiated area of the catalyst is unequal. In addition, light sources may lead to different reaction mechanisms when not using the same lamp. The thermal effects cause promotion or decay in the photocatalytic efficiency; artificial light is fundamental in this efficiency. The Xe and Hg lamps heat up the reactor more than LED light. Finally, the light calibration has to be constant, and the lamps should be replaced when the illuminance has decreased to 70 % of the initial value [15].

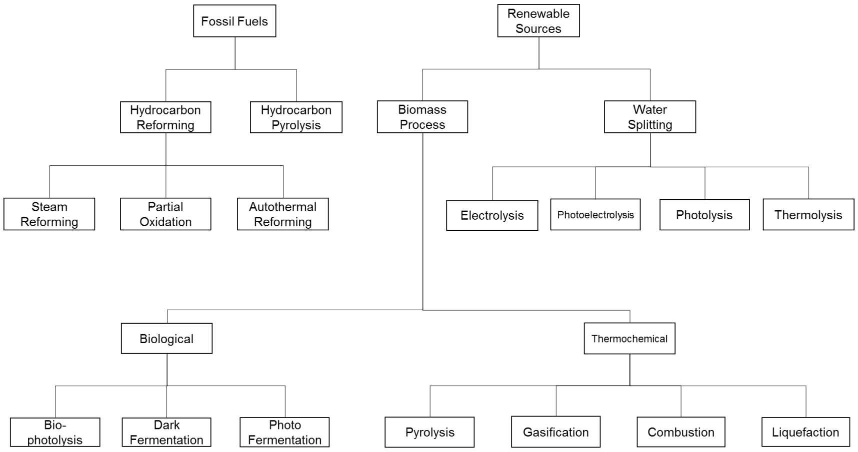

Fig. 1. Methods for producing Hydrogen [8].

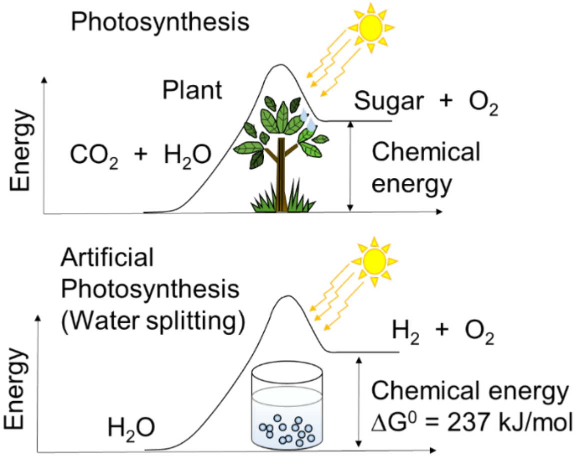

Fig. 2. Natural photosynthesis of green plants and water breakdown as artificial photosynthesis [9].

Fig. 3 describes a single semiconductor as a photocatalyst with HER and OER electrocatalysts on the surface. Initially, a photon is absorbed, producing an excited hole and electron in the valence and conduction bands, respectively. The lifetime is on the femtosecond time scale. After rapid relaxation to the edges of their respective band in femto- to picoseconds, an exciton (electron-hole pair) is separated into free carriers, and the semiconductor-catalyst interface guides the electron and hole to the HER and OER catalysts, generally in nano- to microseconds. Losses of potentials happen at the interface (interfacial loss) and may originate from entropic contributions of electrons and interfacial potential barriers generated by inadequate alignment. From millisecond to second-time scales, the electron/hole are transferred to the electrocatalyst shifts, and the potentials are maintained in steady-state, propitiating the electrochemical redox reactions to produce H_2 and O_2 [12]. Generally, the conversion equipment has a 30 % efficiency for the hydrogen photoconversion reaction [16].

These cells carry out non-spontaneous reactions, and light excitation gives the energy required to facilitate the process. However, if the selection of a semiconductor, as a working electrode, with optimum bandgap and energy levels for both conduction and valence bands, does not afford the Fermi energy required to allow the reaction to proceed spontaneously, an external bias potential should be applied to increase the efficiency of the reaction.

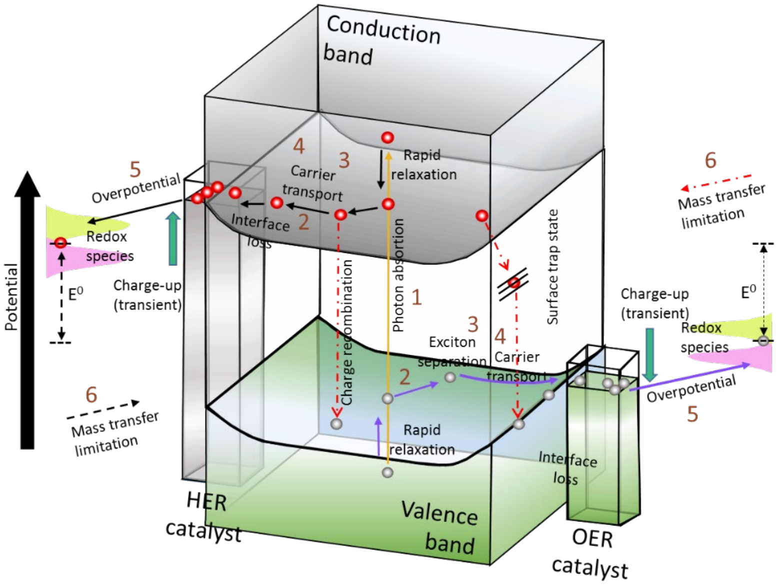

Fig. 3. Photocatalytic water splitting process, each number indicates the order of the photocatalytic process to be successful for overall water splitting. The parameters are **(1)** Photon absorption (Bandgap, Band positions, direct and indirect bandgap, absorption coefficient, optical penetration depth, refractive index, scattering reflection), **(2)** Exciton separation (exciton binding energy, dielectric constant), **(3)** Carrier diffusion (effective mass of carriers, carrier lifetime, carrier mobility, diffusion length), **(4)** Carrier transport (conductivity/resistivity, space charge layer/depletion width, flat band potential, surface state/potential determining ions), **(5)** Catalytic efficiency (electrocatalytic activity exchange current density, IR drop, transfer coefficient, Tafel slope, activation energy, charge transfer resistance) and **(6)** Mass transfer (pH gradient, diffusion "viscosity, effective ion size, activity coefficient") [12].

Transition metal oxides are widely used to perform photoelectrochemical water splitting [3]. A classical experimental setup consists of counter electrode (photocathode is usually Pt) and a semiconductor photoelectrode as working electrode (photoanode) that captures the light. The photoelectrode can be n-type or p-type where it is possible to generate charge carriers (electron/hole pair) (e^-/h^+ respectively) [1]. Following the separation of the generated charge carriers, electrons reduce water to hydrogen while holes oxidize water to oxygen [17]. A good photoelectrode must have: (1) a bandgap energy of approximately 2 eV to be photoactive with sun light and with good light absorption properties, (2) have a suitable position of the band bonds for the evolution of oxygen and hydrogen (0 and 1.23 V vs standard hydrogen electrode (SHE)), (3) efficient charge transport, (4) application of low overpotentials and (5) chemical and electrochemical stability in the aqueous environment under illumination [1,18].

It has also been found that the photocatalyst deposit structure, adhered to the surface of the transparent conductive oxide (TCO) mainly indium tin oxide (ITO) or fluorine dopped tin oxide (FTO), plays a very important role to increase the interaction between the substrate and the electrode. The use of inverse opals, given their structural arrangement generates a high active surface, and has opened a door for improving the efficiency of the reactions where this structure is used. The different methods to synthesize inverse opal structure have allowed to obtain photoelectrodes with enhanced behaviour and performance characteristics. In this review there will be analyzed the different methods to deposit templates on transparent crystalline semiconductors used as electrodes, the different semiconductor metal oxides used for water splitting with the inverse opal structure will be revised, and the different reaction mechanisms in the breakdown of the water molecule to obtain photoelectrochemically H_2 are discussed.

Opals and inverse opals in nature

The word opal comes from Sanskrit (upala meaning precious stone), Latin and Greek translated it as "to see a change of colour". Opals have been known since ancient times as precious stones where their most notable feature is their iridescent greenish-bluish colouration, which is due to the presence of internally trapped contaminants in their crystalline structure. This effect is known as opalescence. Natural opals consist of arrangements of silica spheres with a submicron size between 150 and 400 nm in diameter and with Fe^{3+}, Al^{3+} or Ti^{4+} impurities. Between the silicate spheres, water molecules with a concentration of between 4 and 9 % are trapped, which gives it mechanical stability. The basic crystalline structure that these types of compounds present is the face-centered cubic (FCC), as can be seen in Fig. 4. The density of this type of compound is between 2.0 and 2.2 $g\ cm^{-3}$ and its hardness is between $5\frac{1}{2}$ and $6\ \frac{1}{2}$(Mohs scale) [19].

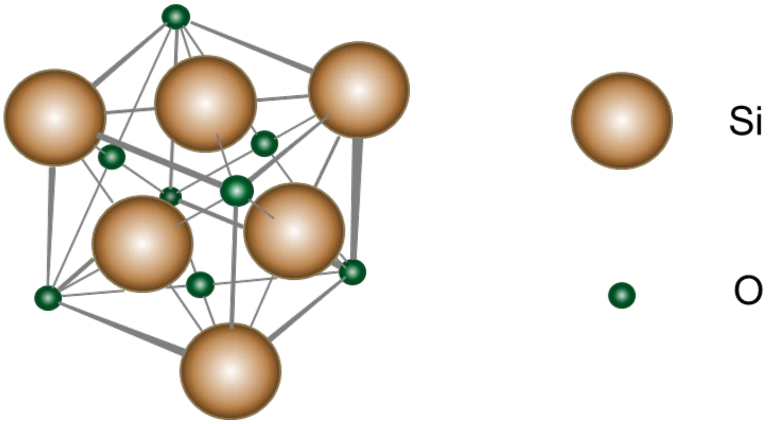

Fig. 4. Description of the general nanostructure of opals that present a Face Centered Cubic (FCC) crystalline structure [19].

In materials science, elements that have their elements with a similar arrangement of atoms to the one described above form compact systems known as opal systems. This arrangement can be built using organic compounds such as polystyrene (PS), polymethylmethacrylate (PMMA) or inorganics such as silicates (SiO_2), where the spaces formed are filled with water that also contains silica. They are produced by the fusion-compression method, obtaining large crack-free films. The films formed use microspheres that are between 100 and 500 nm in diameter that have high porosity and specific optical properties. Fig. 5 shows the opaline arrangement [19,20].

J. Mex. Chem. Soc. **2023**, *67*(4)
Special Issue

ISSN-e 2594-0317

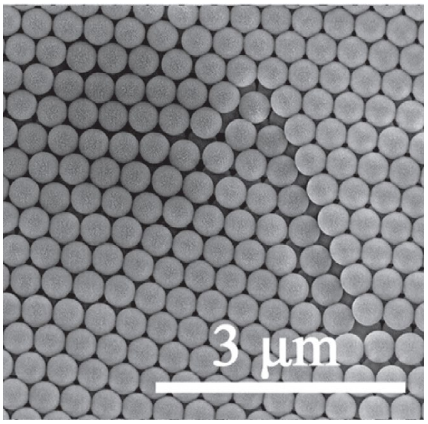

Fig. 5. Scanning electron microscopy (SEM) of the microstructure of the polystyrene template with opal arrangement [21].

The crystal structures of opal compounds include three types of basic geometries as shown in Fig. 6, one-dimensional (1D), two-dimensional (2D) and three-dimensional (3D) crystals [20].

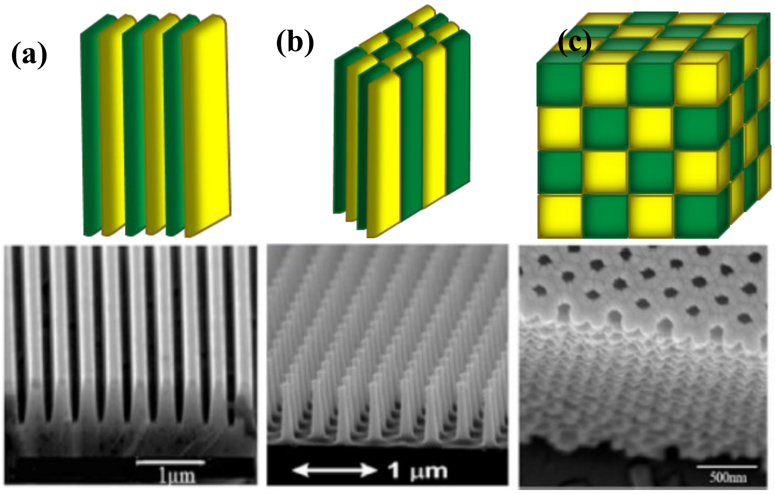

Fig. 6. Schematic representation of the opaline structures **(a)** 1D, **(b)** 2D, **(c)** 3D (green and yellow colors represent the periodicity of the 1D, 2D and 3D structure of the opaline structures) with their corresponding scanning electron microscopy (SEM) image [20].

Inverse opal is an inorganic material with a network of three-dimensional, organized, well-defined pores of different thicknesses. These macroporous and mesoporous structures are interconnected, increasing mass transport through it (Fig. 7). Their arrangement allows to increase the specific surface area, and with it the active sites increase, and the selectivity improves [22]. Applications whose activity or efficiency depend on the surface are benefited by using materials with this geometric arrangement.

To obtain them, a series of steps are required according to Fig. 7. First is the synthesis of the monodisperse polymer, or the silicon colloids, via surfactant-free emulsion polymerization or by the Stöber method [23,24], respectively. These colloids are then crystallized to form a colloidal crystal template or synthetic opal (typically a FCC arrangement with a solid fraction of ~74 % by volume). By different methods, perfectly ordered colloidal

J. Mex. Chem. Soc. **2023**, *67*(4)
Special Issue

ISSN-e 2594-0317

crystals can be obtained from submicrometric spherical colloids, polymers and colloidal silicon, as will be seen later. The opal thus generated is used as a sacrificial template to fabricate inverse opal consisting of a FCC arrangement of air spheres (macropores) in a solid matrix. To obtain the inverse opal, the interstitial void in the colloidal crystal template (26 % volume of the structure) is filled with a solid material via sol-gel, electrochemical, or nanoparticle infiltration. The opal template is finally removed by dissolution or calcination [25].

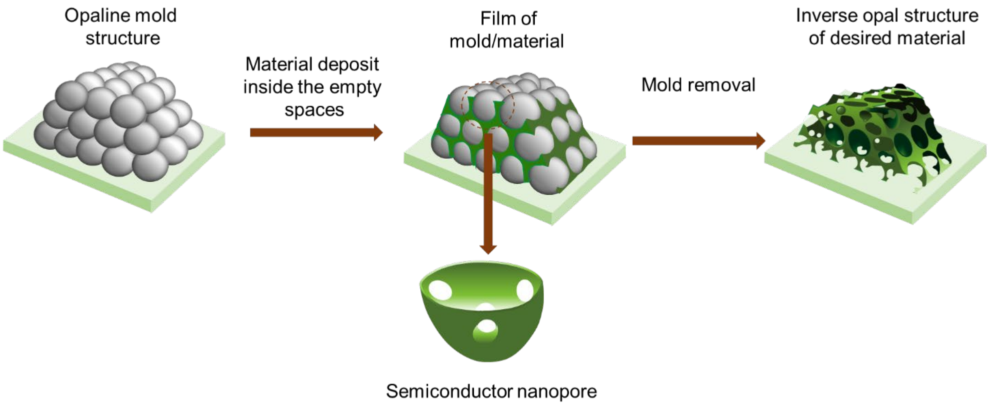

Fig. 7. Schematic diagram of the preparation process and structure of nanoporous films with inverse opal structure [26].

The synthesis of inverse opals helps a greater stability of the material and improves properties that depend on the active surface, allowing them to be used as photonic crystals, materials in catalysis, solar cells, separation of compounds, optical sensors in optoelectronics [27,28], capacitors, gas sensors [29]. Inverse opals are of great interest because they present high and ordered porosity with adjustable periodicity and excellent optical properties [21,30]. In addition, the order of the holes in solid matrices increases the surface area and porosity [31], which increases their catalytic activity by increasing the catalytic sites and improving the diffusion of species in the medium redox pair material inside the electrode in the case of electrochemistry [26]. The average size of the pores depends on the template used (table 2 and table 3) and allows us to determine important factors such as the total pore volume ($V_{Tot} = cm^3\ g^{-1}$), the specific surface area ($a_{s_{BET}} = m^2\ g^{-1}$). Its characteristics help us to explain the amount of light absorbed by the material or photoelectrode, as well as the internal scattering of light [32,33]. There are different methods used to generate these and they will be analyzed in the next section [30].

Table 2. Porosity of inverse opal systems, with semiconductor metal oxides.

Polystyrene spheres diameter (nm)	Inverse opal diameter (nm)	Semiconductor	Reference
113	74 ± 7	ZnO	[34]
~195	~160	$\alpha - Fe_2O_3$	[35]
200	212 ± 22	$CuBi_2O_4$	[36]
280	213 ± 9	Cu	[36]
~285	~235	$\alpha - Fe_2O_3$	[35]
333	235	NiO	[37]
435	335	NiO	[37]
500	450 ± 15	Cu_2O	[36]
500	450 ± 15	$BiVO_4$	[36]

Table 3 shows the fabrication of inverse opal by rapid crystallization at room temperatures and the calcination-induced shrinkage of the opaline matrix. The synthesis method coupled with annealing makes the monodispersity of the holes different from each other. The chemical bath gives us less control of decreasing inverse opal, and ultrasonic spray control shows better control for this board [38].

Table 3. Comparison of pore diameters of ZnO inverse opals fabricated by different techniques [38].

Template	**Template diameter (nm)**	**Synthesis method**	**Inverse opal pore diameter (nm)**	**Pore volume in inverse opal (x10^{-11} μm^3)**	**Reference**
PS sulfonated	~80~120	Ultrasonic spray pyrolysis	~80	0.2144	[39]
Polystyrene (PS)	226	Chemical bath	148±14	1.357	[34]
PS	230	sol-gel	180	2.442	[40]
PS	270, 300 and 350	sol-gel	~250 ~260	6.545 7.362	[41]
PS	300	Oil-water interfacial assembly	280	9.195	[42]

Table 4 is a compilation of the number of spheres of different radius that constitute 1 μm^3 of opaline material. The catalytic behavior of the electrodes improves to have a high surface area, optimal electron pathway, and efficient mass transport. The inverse opal provides a large surface area and interconnected channels for rapid species transport. The sphere size limits area (active sites) and transport of mass (species). The superficial area depends on the number of spheres deposited on the surface of the electrode [43].

Table 4. Number of spheres that fit in a cubic micrometer.

Radius (nm)	**sphere volume (x 10^7 nm^3)**	**Spheres/μm^3**
100	0.419	239
200	3.35	29.8
300	11.3	8.84
400	26.8	3.73
500	52.4	1.91
600	90.5	1.11
700	144	0.696
800	214	0.466
900	305	0.327
1000	419	0.239

Synthesis of opaline (inverse opal)

The structure of the inverse opals depends on the homogeneity of the polystyrene or silicon template. The deposit of high-quality films must have well controlled synthesis parameters such as: hydrophilicity of the substrate surface, angle of inclination, temperature, humidity, solvent and added surfactant. High quality nanostructured photoelectrolytic opals allow easy filling of the precursor solution from the innermost to the outermost part of the opal [36]. Following the general diagram of Fig. 7, each of the stages is described in detail below.

Opal template synthesis

Use of polystyrene as a template

Vertical submersion

The first step for the formation of the template is the self-assembly of the silica or polymer. Monodisperse polymethyl methacrylate (PMMA) can be used as a template. It is synthesized from methyl methacrylate (0.3 or 0.4 L) dissolved in 1.6 L of water. The solution is heated to between 70 and 80 °C with vigorous stirring and under a N_2 atmosphere. To start the polymerization, 1.5 g of 2'azobis (2-methylpropiamidine) dihydrochloride is added rapidly and the reaction is continued for three hours. Finally, the suspension obtained is immediately cooled, filtered through fiberglass, and stored in the absence of oxygen. To carry out the deposit of the polymeric template, the PMMA obtained is dissolved with water up to a volume of 500 mL where the TCO is manually submerged vertically, as seen in Fig. 8. For the formation of the PMMA template sheet, a peristaltic pump is used that works at a flow of 0.3 mL min^{-1}. At this speed, template thicknesses between 5 and 7 µm are obtained. The PMMA template is removed by calcining the electrode up to a temperature of 300 °C with a rate of 2 °C min^{-1} and holding the temperature for 2 hours. Then the temperature is increased from 300 to 400 °C with a ramp of 2 °C min^{-1} and retaining the maximum temperature for 2 hours [25]. The vertical submersion method can also be done with Styrofoam as a template and without using the peristaltic pump for colloidal solution removal. This process is known as simple evaporation [30].

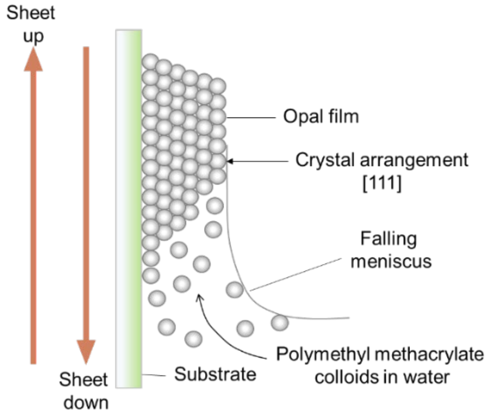

Fig. 8. Formation of an opaline film by the vertical submersion method [25].

Traction method

This method involves submersion using mechanical assistance from the TCO in a polystyrene (PS) suspension. One way to prepare the polystyrene suspension is to add 30 mL of styrene to 150 mL of water with 0.1 M NaOH. The mixture is shaken and washed three times in order to remove the inhibitor. To the mixture is added 0.2 mg of potassium persulfate dissolved in 20 mL of deionized water. The styrene is polymerized at 70° C in an Ar atmosphere for 6 hours, the resulting solution is centrifuged, the PS is kept in deionized water. On the other hand, the TCO is washed with deionized water and absolute ethyl alcohol to be later submerged vertically by the equipment in the manufactured polystyrene dispersion, as can be seen in Fig. 9. It is kept submerged for 3 minutes and then moved through the upper part of the container at a speed of 5 cm min^{-1},

J. Mex. Chem. Soc. **2023**, *67*(4)
Special Issue

ISSN-e 2594-0317

causing the polystyrene to adhere to the surface of the TCO. At the end of this operation, the sheet is dried at 40 °C for 10 min. Then the TCO/PS sheet is submerged again, repeating the operation described above until the appropriate thickness is obtained. A thickness of 6 µm of inverse opal has been obtained by doing three times the aforementioned operation with 1 µm diameter PS spheres in FTO [26].

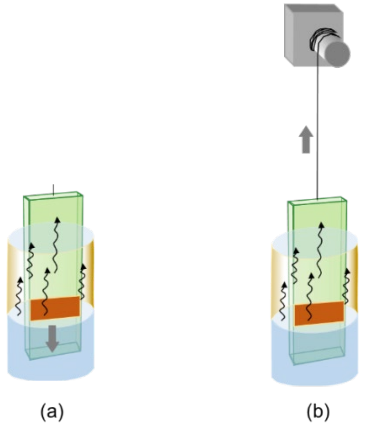

Fig. 9. Vertical deposit **(a)** original configuration, **(b)** combination with a slow lifting of the sample (traction) [19].

Electrophoretic deposit

The speed of formation of colloidal films turns out to be very slow, it can occur in weeks. Due to such a situation, it is not possible to carry out the formation of polystyrene template on an industrial scale. Electrophoretic deposition (EPD) is characterized by the migration of colloidal particles in a liquid that is under the influence of an electric field (electrophoresis) and their subsequent deposition on an electrode or polarized surface as shown in Fig. 10 [44]. The polystyrene is dissolved in a 92.5 % ethanol and 7.5 % water mixture. A 30 % NH_4OH aqueous solution is added to the above solution until a pH of 10.5 is reached so that the polystyrene is negatively charged. The solution is stirred ultrasonically [45]. The use of ethanol as a solvent decreases the decomposition reaction of water and therefore the elimination of bubble formation. For the deposit, a TCO is used, which can be a FTO/glass sheet (anode) and stainless steel as a counter electrode (cathode) (Fig. 10**(a)**). To use this technique, the distance between the two electrodes is generally 1.0 to 2.5 cm and the appropriate voltage is between 3 and 5 $V\,cm^{-1}$ direct current for 5 minutes. The negatively charged polystyrene will be deposited on the anode. For this process, the potential has been imposed by means of pulses of determined duration (Fig. 10**(b)**). The substrate is withdrawn at a speed between 1.0 and 3.0 $mm\,s^{-1}$ and the electrode is placed in a glass desiccator containing anhydrous calcium sulfate [45,46].

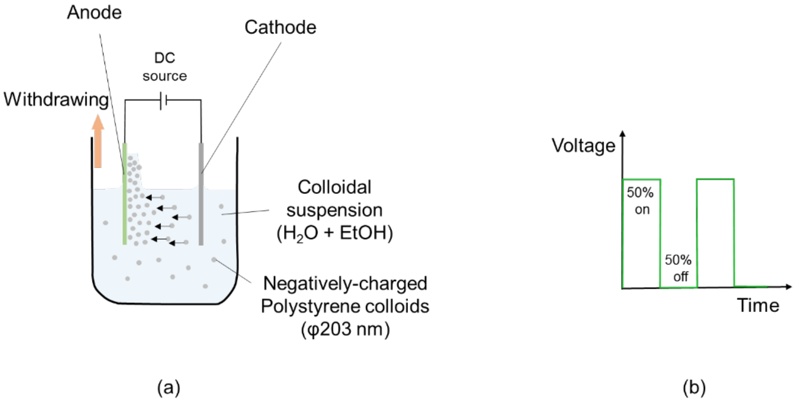

Fig. 10. (a) Schematic diagram of electrophoretic deposition (EPD) of colloidal polystyrene. Anode: FTO/glass or FTO/polyethylene terephthalate (PET), and cathode: stainless steel sheet. **(b)** Schematic of the voltage pulse program [44].

Centrifugal sedimentation method

Another way to obtain the inverse opaline structure is by centrifugal sedimentation, as shown by Nishijima Y., et. al. 2007. Firstly, a colloidal suspension of PS microspheres is made, which is placed in a cylindrical stainless steel container. In the internal base of the reactor, the electrode to be covered is placed submerged in the colloidal suspension. The stainless steel container is centrifuged, as shown in Fig. 11, at 5000 rpm for 10 minutes. It is then dried and annealed at 90 °C for 3 minutes.

If the material in which the gaps will be filled is placed in the colloidal suspension, the gap between the spheres can be filled in the same process, giving rise to the formation of the template and its filling with the desired material in a single process.

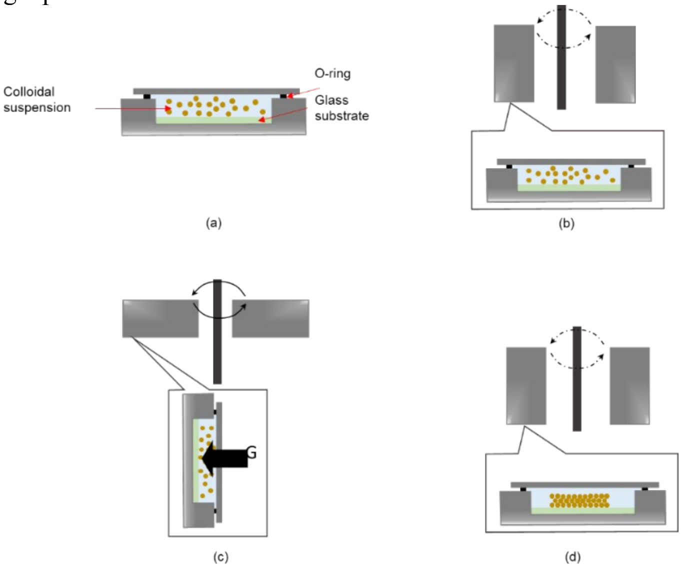

Fig. 11. Diagram of the centrifuged sedimentation process. **(a)** the glass substrate is attached to the bottom of a cylindrical container and the PS colloidal suspension is placed, **(b)** the open part of the container is sealed with a glass slide and the colloidal suspension is allowed to settle by gravity, **(c)** centrifugation begins and the samples are aligned horizontally, and **(d)** centrifugation ends where the cylindrical containers are vertically realigned, obtaining the opal with a uniform thickness on the glass substrate [28].

Coating by centrifugation (spin coating)

This procedure can be done with silicon or PS spheres. To make the dissolution of the polymer, the forces of Van der Waals and the force of attraction of the surface are considered. The concentration of the solution will depend on the diameter of the spheres. Here it is necessary to have a polydispersity < 5 % to obtain a good packing. Fig. 12 shows us the addition of the solution containing PS spheres in a rotating disk with a sample of FTO on its surface. When a high concentration of spheres is used, several 3D layers are formed. Conversely, low concentrations form unwanted spaces and defects in the PS monolayer. The speed of rotation depends on the radius of the substrate and its mass, as the mass decreases the angular speed increases to compensate for the centrifugal force, which becomes less effective. Table 5 shows us how a smaller sphere size and less weight has a greater angular velocity acceleration than when it has a larger size and greater weight. Angular velocity can reach up to 6000 rpm.

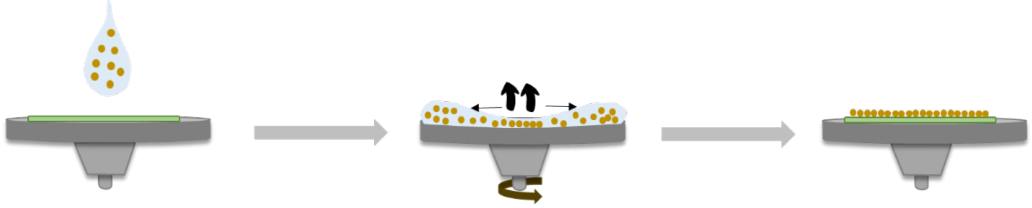

Fig. 12. Self-assembly process of the colloidal crystal, infiltration with the PS sol-gel precursor [46].

Table 5. Optimized rotation parameters for different sphere sizes for a concentration example. Rotation time of 100 s [46].

Sphere size (nm)	**W_r % spheres**	**Rotational speed (rpm)**	**Acceleration (rpm s^{-1})**
100	4.5	6000	6000
300	6.3	6000	400
480	7.1	6000	250
600	7.7	6000	200

Use of monodisperse silicon spheres

For the synthesis of the inverse opal can be from the formation of monodisperse silicon opals [47]. To do this, initially a saturated ethanolic solution of ammonium hydroxide is mixed. It is important to mention that ammonium works as a catalyst for the formation of spherical particles. As a second step, tetraalkyl silicate is added and stirred in an ultrasonic bath in order to keep the particles formed in suspension. Supersaturated silicic acid is then added for condensation to occur. This reaction can be corroborated by the opalescence that the solution takes, where from 1 to 5 minutes SiO_2 spheres are obtained [48]. Different solutions can be used to form the silicon oxide suspension, such as ethylene glycol [49], ethanol-pentylester, methanol:propanol 1:3 mixture [48]. The diameter of the SiO_2 spheres obtained depends on the reaction time, so the shorter the time, the smaller the diameter of the spheres obtained. Among the diameters that have been used for opal synthesis are: 440 nm [50], >500 nm [49], < 0.2 µm [48], 500 nm [51]. The SiO_2 particles settle by gravity for a period of 5 to 20 days on the surface to be used as a support, this allows the growth of the solid phase of the opals, and finally the sediment is dried [50]. The formed opals are joined together giving mechanical stability to the template and controls the void volume of the opal helping in subsequent synthesis such as the formation of inverse opals. Finally, the silicon template is removed using a hydrofluoric acid-based etching procedure [49]. Another way to obtain silicon opals is by the confined convective assembly method (Fig. 13). An aqueous suspension of colloidal silica with a concentration of 10 % by weight and a diameter of 500 nm is synthesized. The colloidal suspension is placed in a stainless steel current collector with a 50 µm gap from the container. The back of the substrate is lifted at 30 $\mu m\ s^{-1}$ while air is added to the meniscus formed at the interface of the substrate and the colloidal suspension. The higher the speed, the less thickness of the silica monolayer and vice versa. The thickness is also controlled by the number of cycles applied, so we have that the greater the number of cycles, the greater the thickness obtained from the monolayer. Finally, the silica opals are removed using hydrofluoric acid [52,53]. This method has the disadvantage of the possible instability of the material used to generate the inverse opal when it is in contact with hydrofluoric acid and that in some laboratories the use of hydrofluoric acid is highly controlled.

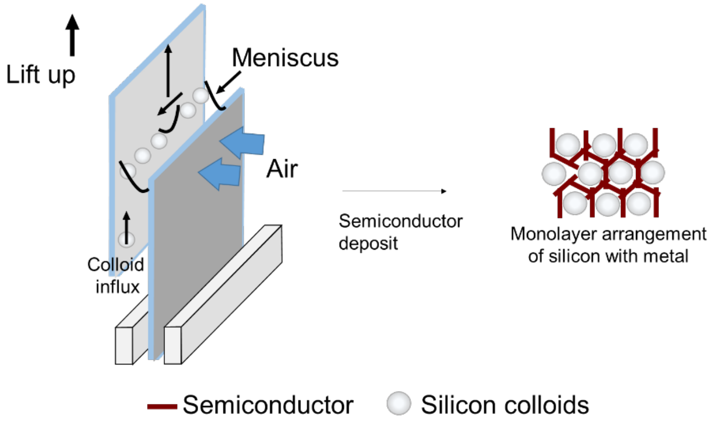

Fig. 13. Two-dimensional hybrid structure diagram using the confined convective self-assembly method [53].

Synthesis of inverse opals from opal systems

Atomic Layer Deposit (ALD)

This technique infiltrates the sacrificial template (PS or SiO_2), in the form of thin films. The inverted structure will be periodically ordered depending on the template obtained on the initially desired surface. Layers with controlled thickness can be obtained from water vapor precursors and substrates that can give rise to many materials with their own structural characteristics. The infiltrated structures are obtained at relatively low temperatures below 85 °C (lower than the glass transition temperature of PS 95 °C) to avoid damaging the template. Cycles are used where the substrate is dissolved in a chamber at a temperature above 80 °C (as shown in Fig. 14**(a)**), and the plate containing the opaline structure is located in another chamber at a temperature of 85°C and pressure of 5×10^{-1} mbar. Nitrogen is used as stripping gas and it is found in containers at low pressures (9×10^{-2} mbar). The residence time of each cycle can last up to 60 minutes and have a heating rate of 1 °C $\min^{-1}$ [54,55]. On the other hand, Scharrer M. et al. (2005) have used reaction times of 2.0 s per 30 s N_2 purge followed by 4.0 seconds H_2O exposure and again another N_2 purge. This technique is easy to maintain since it does not require frequent cleaning, the generated residues are the chemical solutions used for the synthesis, therefore it generates low contamination; besides this technique controls the thickness of the films generated at the nanometric level and is easily deposited in a rough surface [56]. Finally, it is recommended to remove the polystyrene template calcining at 550°C for 30 minutes [57].

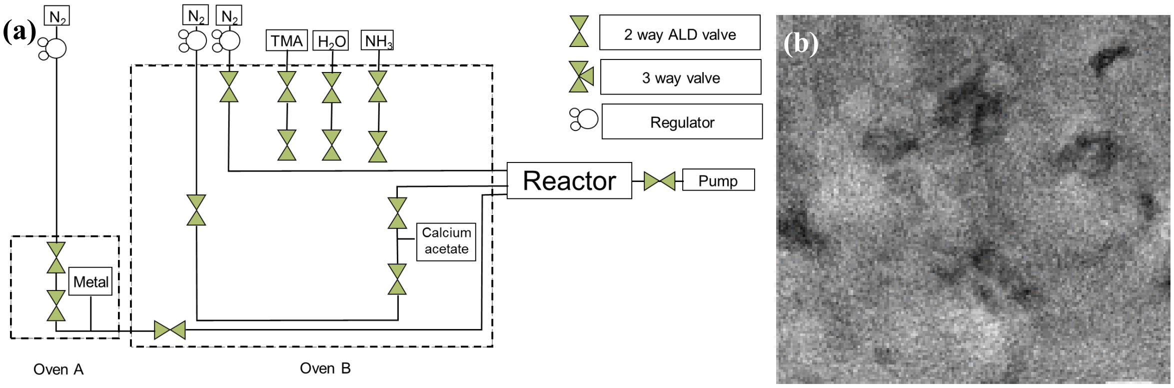

Fig. 14. (a) General diagram of the atomic layer deposition (ALD) method. **(b)** transmission electron microscopy (TEM) micrograph of the $Mg_{0.25}Ca_{0.75}O/Si_3N_4$ membrane obtained by ALD [58].

Electrodeposit

Reversible periodic potential (pulses)

The current/potential is applied in the form of modulated waves (Fig. 15**(b)**) controlling the on and off time (t_{on} and t_{off}, respectively). The duty cycle helps control the electrochemical process that affects diffusion layer, grain size, and nucleation. This is defined as:

$$duty\ cicle\ (\%) = \frac{t_{on}}{t_{on} + t_{off}} x100$$

t_{off} helps the formation of new nucleation sites, decreasing the porosity and roughness of the deposit. The reverse pulse is when short anode pulses are applied alongside the cathode pulse (Fig. 15**(c)**). The anodic pulse causes electro-oxidation to occur on the deposited surface, removing impurities to obtain a smoother surface [59].

Conductive material or electrode is required to make the electrodeposition which is submerged in a neutral aqueous bath. The reaction is carried out in a three- electrode cell with FTO being the most common working electrode, a Pt sheet as the counter electrode, and Ag/AgCl the reference electrode for aqueous media (Fig. 15**(a)**). Before carrying out the deposition reaction the FTO is rinsed with deionized water and dried in a flow of air. With this technique it is recommended to carry out a cyclic voltammetry to the precursor solutions to know their behavior

J. Mex. Chem. Soc. **2023**, *67*(4)
Special Issue

ISSN-e 2594-0317

in the FTO, verifying that there are no alternate reactions in the working electrode once the potential has been selected based on the above. An anodic overpotential is applied followed by a cathodic overpotential for a certain time in each process, being only a few seconds as shown in the Fig. 15b. With the anodic overpotential, the elimination of the excess metal deposited on the working electrode is ensured [60], likewise, it allows the diffusion of the metallic ion from the electrolyte solution towards the working electrode, decreasing the concentration gradient when the cathodic potential is applied again [61]. The number of repetitions applied (cycles) will indicate the thickness of the inverse opal obtained. The greater the cathodic overpotential, the faster the cathodic deposition will be and the more anodic the dissolution of the deposited undesirable metal. The correct selection of the time of the cathodic and anodic process as well as its potential are crucial factors for the adequate deposition of the desired metal within the void space of the opal structure. The calcination of the template allows obtaining the structure of the inverse opal [60]. Fig. 15**(d)** shows electrodeposited hematite by SEM with inverse pulse voltage on a glass support and Ni opal on its surface [62].

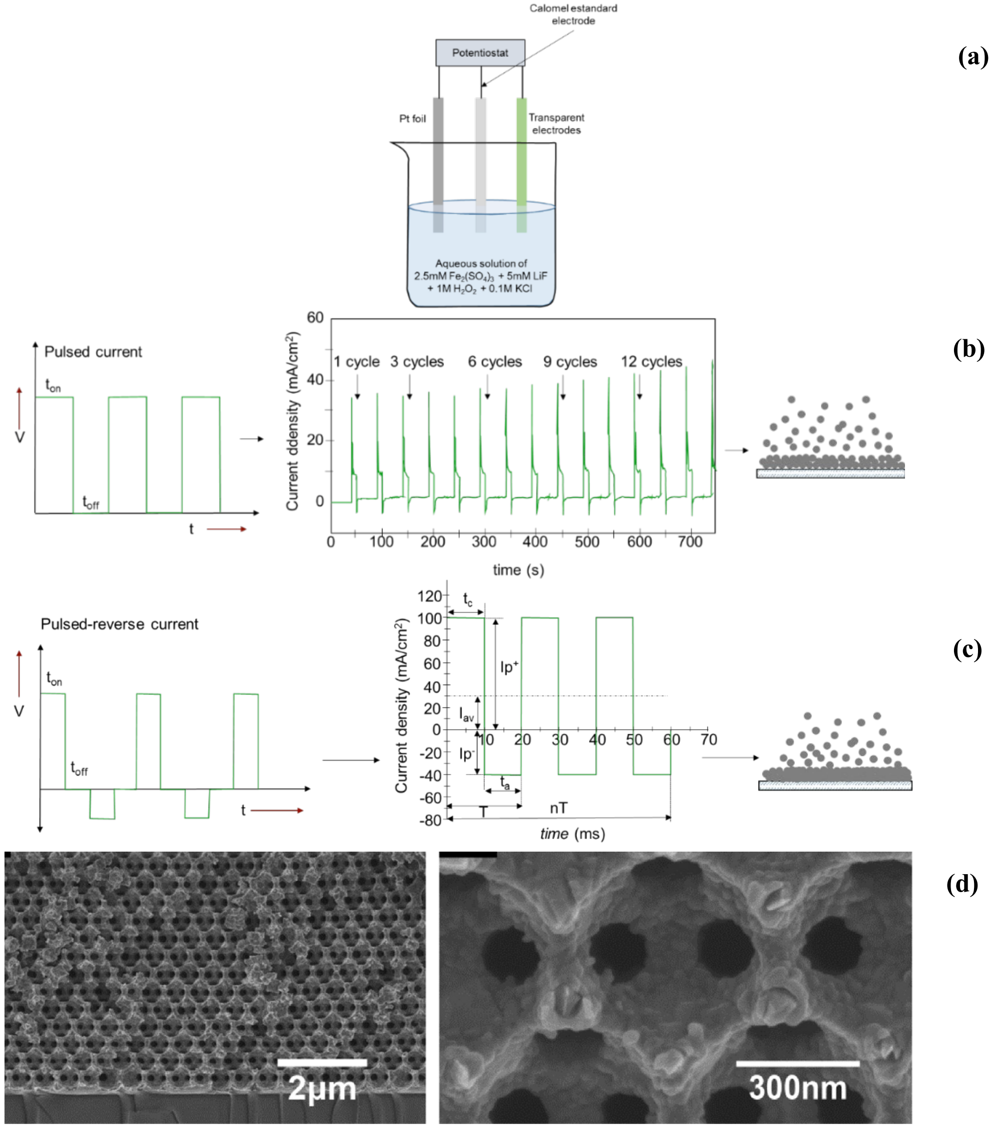

Fig. 15. (a) Three electrode electrochemical cell with FTO working electrode, Pt counter electrode and standard calomel electrode. **(b)** Scheme of pulsed electrodeposition and **(c)** and reverse pulse with the expected growth process. I_{p^+} is peak positive current density, I_{p^-} peak reverse current density, I_{av} average current density, T cycle time, t_{c} cathodic time, t_{a} anodic time [59,61,63]. **(d)** SEM image of hematite deposited by reverse pulse on a glass slide coated with Cr and Au and Ni opal on its surface [62].

With fixed potential

Generally, both the applied overpotential and the composition of the electrolyte in the tank are controlled. In this technique the surface is subjected to a constant potential (Fig. 16**(a)**), which governs the shape of the crystal below or near the conditions of thermodynamic equilibrium. Above equilibrium (high overpotential) the shape of the crystal is dominated by mass transport and surface properties. Under these conditions, metal ions are consumed faster than their transport speed, so crystal growth is limited by the diffusion of these ions. For electrodeposition, a three-electrode electrochemical cell is used (Fig. 15**(a)**). A semiconductor crystal such as the FTO with PS template can be used as the working electrode. This semiconductor is rinsed by sonication for 20 minutes in deionized water and then dried under N_2 flow. Graphite or Pt that has been rinsed with deionized water beforehand is used as the counter electrode. The reference electrode is Ag/AgCl with a 1 M KCl solution [64]. It is necessary to apply the cyclic voltammetry technique to know the potentials in which the metal or metal oxide deposit occurs from the solution in which it is prepared [65]. The calcination of the template allows obtaining the structure of the inverse opal deposited (Fig. 16**(b)**) (varying the potential low potential and high potential).

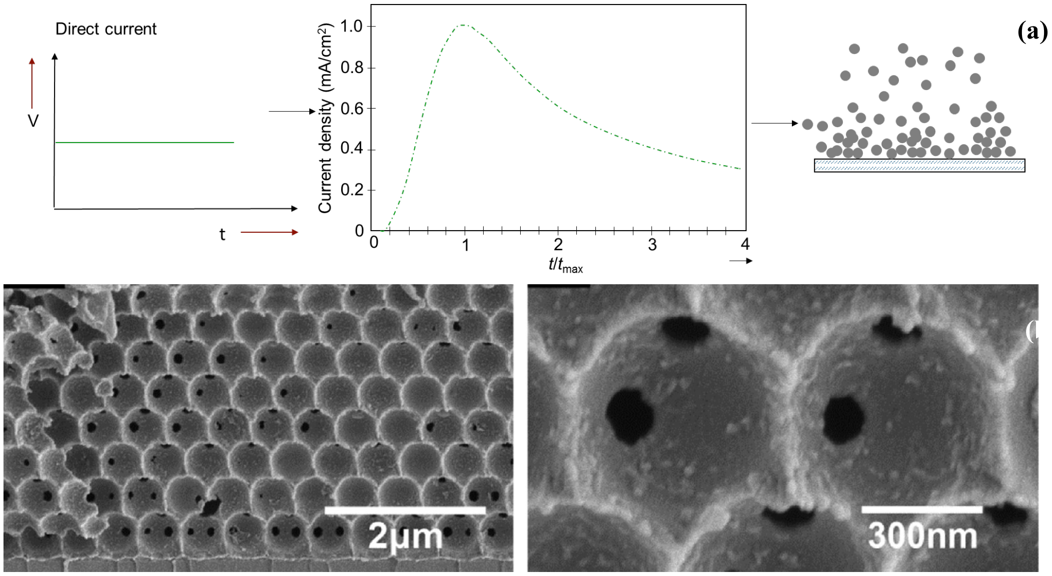

Fig. 16. (a) Scheme of electrodeposition at constant voltage and the expected growth process **(b)** SEM image of hematite nanoparticles deposited at fixed potential on Ni inverse opal which in turn was deposited on a glass slide that initially it is coated with Cr and Au on its surface [59,62,66].

Sol-gel

The manufacture of inverse opals by this method requires high temperatures and allows easy control of the volume of the precursor. In addition, the reaction conditions that are used are easy to prepare. The precursor is prepared by sol-gel and is cleaned with distilled water. It is infiltrated into the template by the submersion method, as shown in Fig. 17. This allows the nanoparticles to be deposited on the walls and cavities of the template. The dipping process should be repeated one or two more times to ensure complete infiltration of the template into the precursor solution. Finally, it is calcined to eliminate the template [67]. Table 6 is summarized the methods of obtention of inverse opal in this review and its differences.

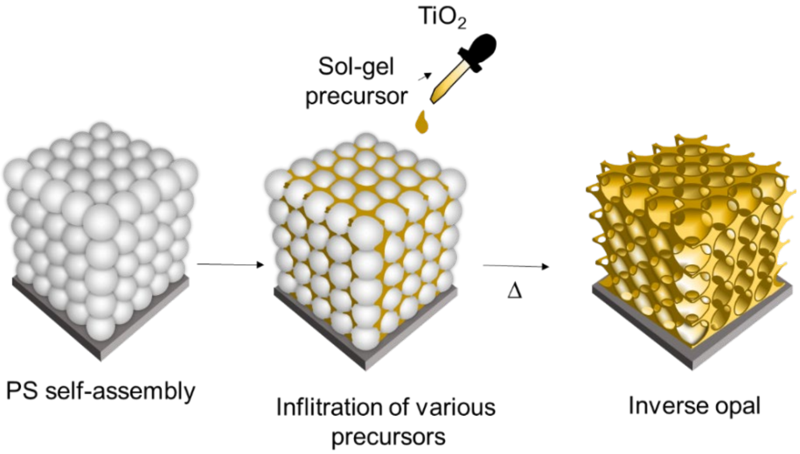

Fig. 17. Scheme of the manufacture of inverse opals by the sol-gel method [67].

Table 6. Synthesis of inverse opals from opal systems.

Method	Template	Characteristics	Conditions
Atomic Layer Deposit	PS or SiO_2 thin films	Water vapor precursors and substrates in pressure chambers (0.5 mbar)	Conductive material inside the chamber and a fluid of N_2 carrier gas at 85°C with water vapor precursor. Finally calcination is applied.
Electrodeposit (reversible periodic potential "pulses")	PS	Three-electrode cell FTO - working electrode Pt sheet - auxiliar electrode Ag/AgCl – reference electrode	Conductive material submerged in a neutral aqueous bath and apply 1° anodic overpotential (large time) 2° cathodic overpotential (short time). Apply calcination.
Electrodeposit (fixed potential)	PS	Three-electrode cell FTO - working electrode Pt or graphite - auxiliar electrode Ag/AgCl – reference electrode	Conductive material submerged in a neutral aqueous bath and know the potentials apply an overpotential which the metal or metal oxide deposit occurs. Apply calcination
Sol-gel	PS or SiO_2	Crystal material	Precursor in sol-gel is infiltrated into template by the submersion and heated for evaporation and calcination.

Materials with inverse opal structure of interest in photoelectrochemical water-splitting

In this section we will focus on the materials that have been used to develop photoelectrodes for water-splitting and where the inverse opal structure has been used.

J. Mex. Chem. Soc. **2023**, *67*(4)
Special Issue

ISSN-e 2594-0317

Zinc oxide (ZnO)

The ZnO photoelectrode is classified as an *n*-type binary semiconductor due to the interstitial zinc and vacant oxygen atoms in its crystal lattices. It has been studied as a photodetector, photodiode, gas sensor, solar cells, supercapacitors, optoelectronic and piezoelectronic equipment, batteries for energy or hydrogen storage, biosensors to capture biological molecules (glucose and cholesterol) in aqueous solutions [68]. Their interest as a photocatalyst is due to their environmentally friendly, low cost, low toxicity, and efficient photoelectrocatalytic behavior [69,70]. It has a band gap of 3.37 eV (368 nm) [17] and presents different colors when annealed at different temperature ranges (100-400 °C dark color, ~550°C transparent) [71]. It presents an excellent electron mobility (up to ~ 1000 $\mathrm{cm^2\ V\ s^{-1}}$) [69] being higher than that of $\mathrm{TiO_2}$. It has a great efficiency in the transfer of the electron, making the lifetime of the $\mathrm{e^-/h^+}$ pair longer and decreasing the recombination rate. It absorbs 4 % of the solar spectrum (Fig. 18), which means that its photoactivity in the visible is very small. The minimum conduction band has an energy of -0.31 V vs NHE and the maximum valence band is 2.89 V vs NHE [4,72]. The main crystalline structure used in photoelectrochemistry is wurtzite, which presents a hexagonal close-packed crystalline structure (hcp) with space group C6cmc (Fig. 19**(a)**). It has planes composed of coordinated $\mathrm{O^{2-}}$ and $\mathrm{Zn^{2+}}$ tetrahedral ions stacked along the *c* axis (Fig. 19**(b)**). The size of the wurtzite edges is *a* = *b* = 0.32 nm and *c* = 0.52 nm [69,73] and it has a binding energy of 1021 eV for Zn $2p_{3/2}$ and 1044 eV for Zn $2p_{1/2}$ [74]. Its structure presents the following crystallographic planes (100), (002), (101), (110), (103) and (112) [75]. The compact hexagonal structure can intersect with another hcp to form tetrahedral arrangements, regularly occupied by four Zn atoms, and hexagonal arrangements with twelve atoms, as shown in Fig. 19**(c)**. Crosslinking makes the crystal thermodynamically stable. The unit cell of this type of compounds exhibits two types of low index surfaces: (1) polar surfaces $(00\bar{1})$ terminated with oxygen and (001) terminated with zinc and, (2) nonpolar surfaces $(\bar{1}00)$. It has a minimum conduction band with energy of -0.31 V vs. NHE and maximum valence band of 2.89 V vs. NHE allowing the oxidation of water [76,77]. ZnO has a low enthalpy of formation, causing it to present vacancies when oxygen desorption occurs near the surface of the crystalline system, thus we have:

$$\mathrm{Zn-O-Zn} \longrightarrow \mathrm{Zn-V_O-Zn} + \frac{1}{2}\mathrm{O_2}$$

$\mathrm{V_O}$ is oxygen vacancy.

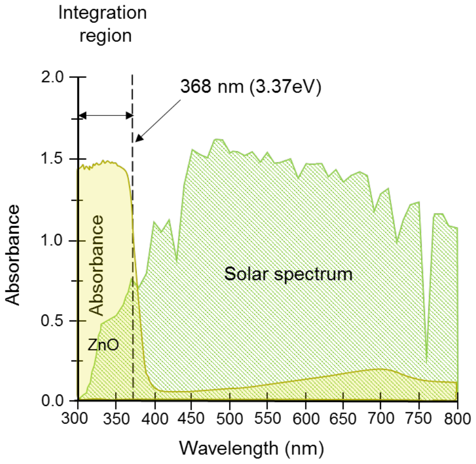

Fig. 18. Solar UV-Vis absorption spectrum of zinc oxide [16].

J. Mex. Chem. Soc. **2023**, *67*(4)
Special Issue

ISSN-e 2594-0317

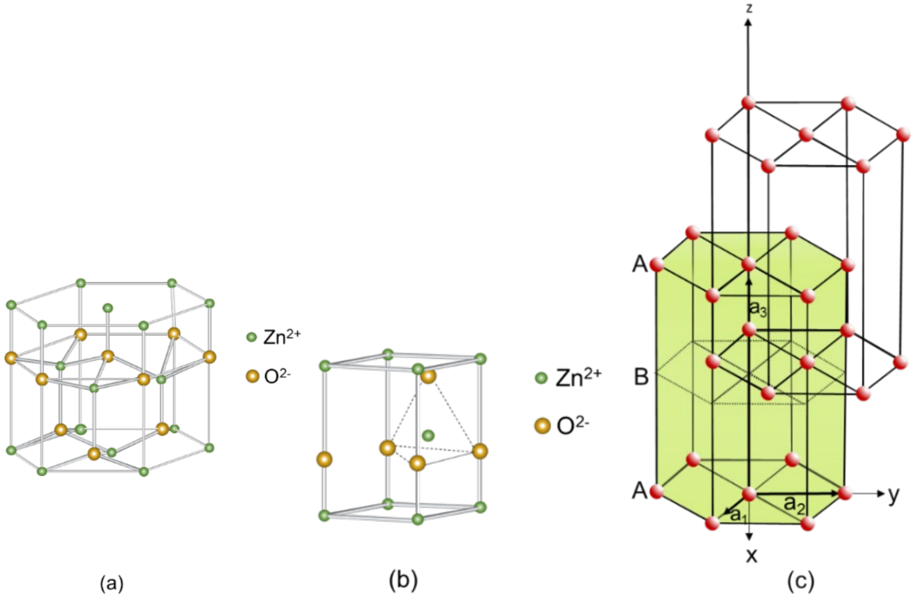

Fig. 19. (a) Close-packed hexagonal crystal structure of wurzite (ZnO) **(b)** ZnO tetrahedral crystal and **(c)** Penetration of two hexagonal structures for the formation of a close-packed hexagonal structure [69,77].

The amount of oxygen that is near the surface in the crystal arrangement depends on the morphology of the ZnO on the conductive surface. Table 7 shows that said morphology is subject to the electrolyte used for anodizing. The amount of oxygen will indicate the number of vacancies formed in the crystalline arrangement, this in turn influences the forbidden band of the photoelectrode [68], since the number of vacancies that trap electrons photogenerates changes, causing the recombination of the e^-/h^+ pair to decrease or increase. The greater the number of vacancies, the greater the charge transport, the greater the photocurrent density and consequently, the greater the oxidation reaction of water [74]. The vacancies formed by oxygen have an energy of ~1 eV on the edge of its valence band [17].

Table 7. Morphologies and bandgap of ZnO nanostructures reported in the literature, obtained by electrochemical anodization using various types of electrolytes [68].

Electrolyte (aqueous solution)	Morphology	Band gap (eV)	References
$NaOH + NH_4F + H_2O + C_2H_6O_2$	Nanowires	[3.19 - 3.22]	[68]
$H_2O, NaOH, H_2C_2O_4$ or $CH_3OH + HF$	Nanopores	[3.10 - 3.87]	[78–82]
$C_2H_5OH + H_2SO_4, C_2H_5OH + H_3PO_4, (NH_4)_2SO_4$ or $(NH_4)_2SO_4 + NaOH$	nanoflakes	---	[83–86]

$NaOH, C_2H_5OH + NaOH, C_2H_5OH + H_2C_2O_4$, $CH_3OH + HCl$, $C_2H_5OH + HNO_3$ or $C_2H_5OH + HF$	nanoflowers	~3.50	[82,84,85]
$(NH_4)_2SO_4$ or $(NH_4)_2SO_4 + NH_4Cl$	Nanosheets	---	[87]
$KHCO_3, NaHCO_3, NH_4CO_3, NH_4F$, $C_2H_5OH + KHCO_3, CH_3OH + HF$ or HF	Nanowires	3.19 - 3.50	[82,85,88–93]

It has also been found that using different annealing temperatures can modify the ZnO electrode. For example, annealing at 700 °C helps the generation of p-type ZnO by increasing defects in the crystal grain arrangement. At this temperature there is a maximum concentration of interstitial oxygen (O_i) and a minimum concentration of interstitial Zinc (Zn_i). Zinc acts as a donor (V_O, Zn_i), while oxygen acts as an acceptor (V_{Zn}, O_i) [94].

In Table 8 it can be observed the size in diameter of the ZnO inverse opal due to the use of different methods of depositing the polystyrene template. By the sol-gel method, from polystyrene spheres of 300 nm in diameter, the ZnO inverse opals obtained have a pore size of between 250-260 nm. By the oil-water interfacial assembly method, inverse opals obtained from ZnO have a pore size of 280 nm in diameter [38]. In Fig. 20 we see the inverse opal structure of ZnO with great softness and quality in its structure [95]. Table 9 shows the behavior of different types of ZnO nanodeposits with the corresponding current density.

Table 8. Comparison of the pore diameter of the ZnO inverse opal [38].

Template	Template diameter (nm)	Synthesis method	Inverse opal pore diameter	References
Polystyrene (PS)	270, 300 and 350	sol-gel	~250-260	[41]
PS	300	Oil-water interfacial assembly	280	[42]
PS	230	sol-gel	180	[40]
PS Sulfonated	~80-120	Ultrasonic spray pyrolysis	~80	[39]
PS	226	Chemical bath deposit	148 ±14	[34]

J. Mex. Chem. Soc. **2023**, *67*(4)
Special Issue

ISSN-e 2594-0317

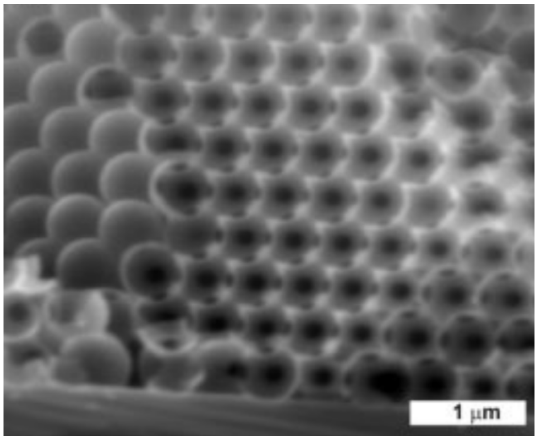

Fig. 20. SEM image of inverse opal of ZnO from opal of polystyrene spheres of 500 nm in diameter [95].

Table 9. Comparison of the current density of different ZnO electrodes with different crystal forms.

Morphology	Current density	Electrolyte	Vs. Ref. Electrode/CE	References
Overlapping nanowires	57 μA cm^{-2}	0.5M Na_2SO_4	Ag/AgCl Pt	[96]
Nanorods	27 μA cm^{-2}	0.5M Na_2SO_4	Ag/AgCl Pt	[96]
Nanoflowers	60 μA cm^{-2}	1M Na_2SO_4	Ag/AgCl Pt	[73]

Nickel sulfide (NiS)

Nickel sulfide is a p-type semiconductor [97]. Metallic sulfides are attractive because of their abundance in the earth, cheap, active in visible light, and small bandgap [98]. They present good thermal and mechanical stability, excellent redox reversibility, conductivity and capacitance. Nickel sulfides consist of different compounds with different phases and stoichiometry such as: NiS, Ni_3S_2, NiS_2, $Ni_{3+x}S_2$, Ni_3S_4, Ni_6S_5, Ni_4S_{3+x} and Ni_7S_6. The most used phases are: Ni_3S_2, Ni_3S_4, NiS_2 and NiS. NiS (also represented as $Ni_{1-\delta}S$) presents two different crystalline arrangements: $\alpha - NiS$ (hexagonal nickeline phase) (Fig. 21**(a)**) with six sulfur atoms and one nickel atom and with cell parameters a = 0.34422 (3) nm, c = 0.53588 (3) nm, α = β = 90° and γ = 120° [99]. $\beta -$ NiS (rhombohedron millerite phase) (Fig. 21**(b)** and Fig. 21**(c)**) with five coordinated sulfur atoms and one nickel atom. Of these two structures, $\beta -$ NiS has a better catalytic efficiency than $\alpha -$ NiS. $\alpha -$ NiS is obtained by annealing at 200 ℃ at a ratio of 0.95:1.05 while at 400 ℃ $\beta -$ NiS is obtained at a ratio of 0.99:1.01 [100]. The binding energy of $\alpha -$ NiS for S $2p_{3/2}$= 161.65 eV and of $\beta -$ NiS is S $2p_{3/2}$= 161.7 eV. The α and $\beta -$ NiS have the same binding energy for Ni $2p_{3/2}$= 853.1 eV [99]. The absorption spectrum of $\beta -$ NiS is 4.8 eV. The bandgap of $\alpha -$ NiS is 0.8 eV and of $\beta -$ NiS is 1.0 eV. Likewise, the conversion efficiency of the incident photon to electron (η) of $\alpha -$ NiS is 5.2 % and for $\beta -$ NiS it is 4.2 % and its filling factor is 67 % and 63 %, respectively. NiS parameters: (100), (101), (102) and (110) [101]. Parameters of $\alpha -$ NiS: (100), (002), (101), (102), (110), (103), (200), (112), (004) and (202). Parameters of $\beta -$ NiS: (110), (101), (300), (021), (220), (211), (131), (410), (401), (321), (330), (012), (122), (600) and (042) [102]. The $\alpha -$ NiS presents a better photocatalytic activity than the $\beta -$ NiS due to the band edge potential of 1.83 eV that influences a higher generation of e^- y h^+ [98]. Fig. 22 presents the absorption spectrum of $\alpha -$ NiS and $\beta -$ NiS. This compound has been used mainly in the hydrogen evolution application and as cathodes in lithium batteries.

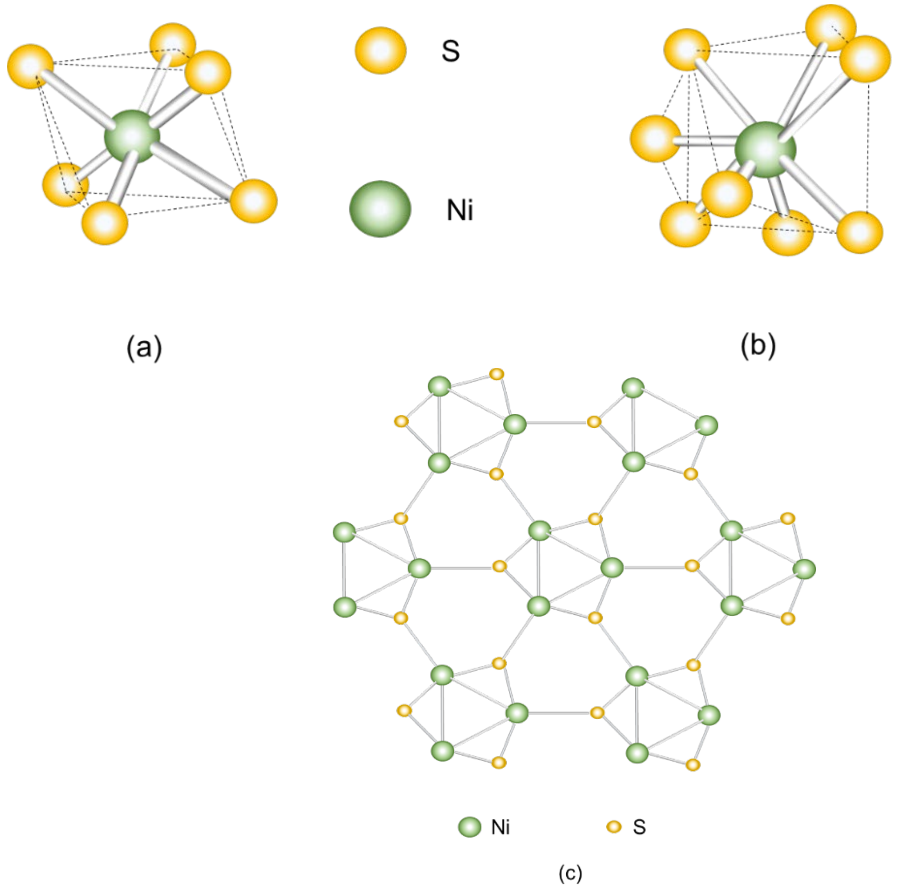

Fig. 21. Crystal structure of **(a)** nickeline (α − NiS), **(b)** millerite (β − NiS) [103] and **(c)** millerite viewed along the [001] plane [100].

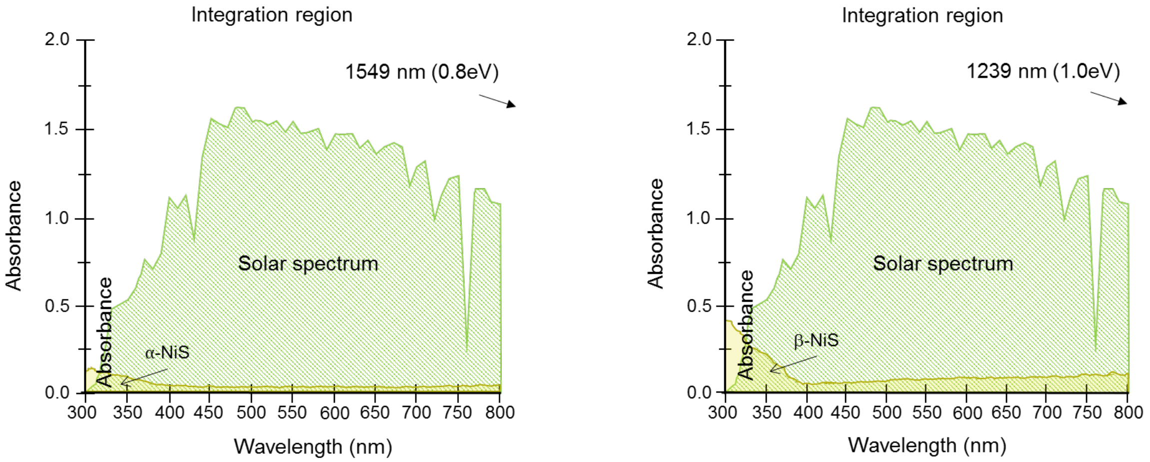

Fig. 22. Solar absorption spectrum of UV-Vis **(a)** α − NiS and **(b)** β − NiS [102].

J. Mex. Chem. Soc. **2023**, *67*(4)
Special Issue

ISSN-e 2594-0317

For its synthesis, the following is sought: (1) to increase the intrinsic activity of the oxygen evolution reaction, optimizing the Gibbs free energy by the absorption of $\mathrm{OH^-}$ groups and avoiding the capture of chemical agents. Thus, using 1.0 M KOH, a Faradaic redox reaction of $\mathrm{M^{2+}/M^{3+}}$ ($\mathrm{M = Mo, Cu, W, Co}$, Ni and Fe) occurs from the metal sulfide that couples with the $\mathrm{OH^-}$ group present in the electrolyte, occurring:

$$\mathrm{MS + OH^- \rightarrow MSOH + e^-}$$
$$\mathrm{MSOH + OH^- \rightarrow MSO + H_2O + e^-}$$

(2) increase the electronic conductivity and density of the electrochemical active sites, and (3) optimize the mass transport properties [104].

One way to deposit NiS on a glassy conductive material is by the reversible periodic potential method (Section reversible periodic potential "pulses"). An aqueous solution is prepared containing 50 mL of 50 mM $\mathrm{NiCl_2 \cdot 6H_2O}$ and 1.0 M thiourea. Thiourea is electrochemically inert on the FTO surface. The cathodic deposition is carried out with an overpotential of -0.9 V for 24 seconds and immediately the anode overpotential of 0.1 V is applied for a time of 6 seconds, this operation is repeated 10 times to obtain an adequate thickness. An increase in instantaneous anodic current is attributed to the presence of metallic Ni deposited on the electrode, an increase in instantaneous cathodic current during the anodic process indicates the presence of $\mathrm{Ni^{2+}}$ on the FTO electrode surface [60].

In table 10 we can see the influence of morphology and structure on electrochemical behavior due to the increase in surface area and roughness. As the surface area increases, the active sites increase and the electrolyte diffusion pathway and charge transport decrease [105]. The capacitance concept bifurcates into two types according to its charge storage mechanisms; one is electrical double-layer capacitance C_{dl}, generated from charge separation at the electrode/electrolyte interface and determined by the effective surface area and the dielectric constant of the electrolyte, and pseudocapacitance C_p, generated from fast faradic reactions of the electrode material. Pseudocapacitance is produced from a bulk process, whereas double-layer capacitance works from a surface process. The specific capacitance indicates the charge/discharge capability and its dependence on a large surface area, high specific capacitance means a large reaction area [106]. Fig. 23 presents an SEM micrograph of NiS inverse opal electrodeposited on FTO.

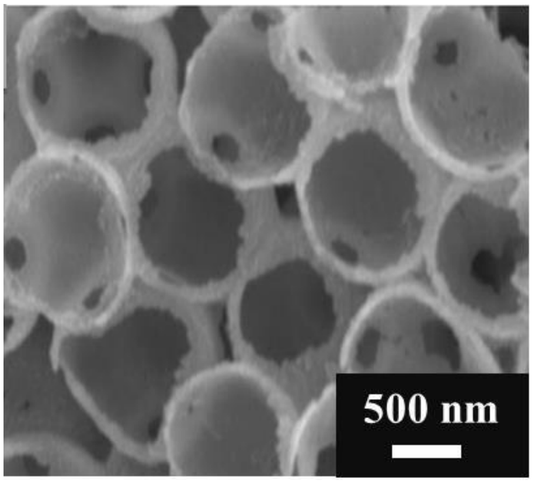

Fig. 23. SEM image of NiS inverse opal deposited on FTO surface [26].

J. Mex. Chem. Soc. **2023**, *67*(4)
Special Issue

ISSN-e 2594-0317

Table 10. Comparison of the specific capacitance (C_m) of different NiS electrodes with different crystal forms [105].

Morphology	**Current density**	**Electrolyte**	**C_m($F\ g^{-1}$)**	**References**
Microflowers	$1\ A\ g^{-1}$	3 M KOH	1122.7	[105]
Graphene nanospheres / NiS films	$0.5\ A\ g^{-1}$	6 M KOH	775	[107]
Hollow spheres	$4.08\ A\ g^{-1}$	2 M KOH	927	[108]
Nanoparticles	$1\ A\ g^{-1}$	6 M KOH	845	[109]
Nanosheets	$2.5\ mA\ cm^{-2}$	2 M KOH	527	[110]
Inverse opal	$1.25\ mA\ cm^{-2}$	0.1 M LiI; 0.03 MI_2; 0.3 M 1,2-dimethyl-3-propylimidazolium iodide; 0.5 M 4-tert-butyl pyridine; 0.1 M guanidinium thiocyanate in acetonitrile		[26]

Copper (I) oxide (Cu_2O)

It is a very abundant, environmentally friendly, and low-cost material, so its derivatives share this characteristic [30]. Cu_2O has a bandgap of ~2.1 eV which causes a large part of the solar spectrum to be absorbed (Fig. 24).

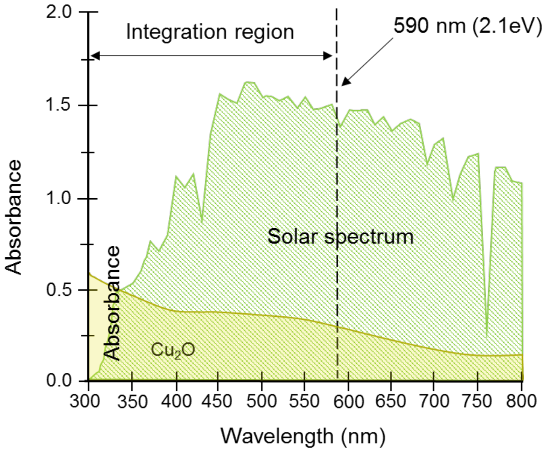

Fig. 24. Solar UV-Vis absorption spectrum of copper (I) oxide [111].

It has a maximum theoretical photocurrent density of -14.7 mA cm^{-2} at AM 1.5 conditions. The solar to hydrogen conversion efficiency is 18.1 %. It presents a favorable position of the conduction band with respect to the hydrogen reaction potential. It has a low stability against photodegradation. Under illumination, the electrons that are in the solid-liquid interface reduce the Cu_2O semiconductor to Cu metal, decreasing the generated photocurrent [112,113]. In Fig. 25 we see two crystalline structures for cuprite (Cu_2O). **(a)** Structure of cuprite, the copper atom is coordinated by two oxygen atoms and each oxygen atom surrounded by a tetrahedron of copper

J. Mex. Chem. Soc. **2023**, *67*(4)
Special Issue

ISSN-e 2594-0317

atoms. It has a body-centered cubic (BCC) arrangement where the special positions of the copper atoms are at (0.25, 0.25, 0.25); (0.75, 0.75, 0.25); (0.75, 0.25, 0.75); (0.25, 0.75, 0.75) and the special positions of the oxygen atoms are at (0, 0, 0); (0.5, 0.5, 0.5). **(b)** The special positions of copper are at (0, 0, 0); (0.5, 0.5, 0); (0.5, 0, 0.5); (0, 0.5, 0.5) and the special positions of oxygen are at (0.75, 0.75, 0.75); (0.25, 0.25, 0.25) [65].

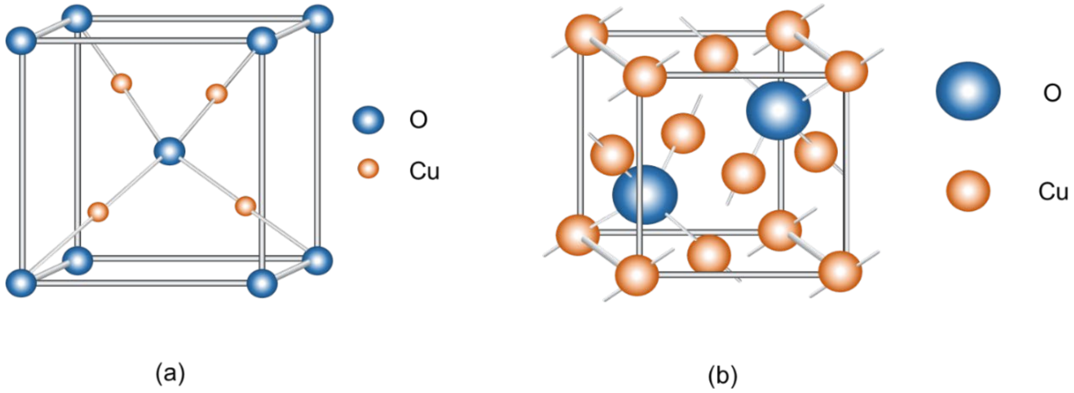

Fig. 25. Cu_2O unit cell. The cubic structure has an array parameter of 0.42696 nm. It features two interpenetrating cubic arrangements. One is BCC and its arrangement is occupied by oxygen atoms **(a)** and another is FCC and its points are occupied by copper atoms **(b)** [65].

In the synthesis of inverse opals, Cu_2O presents greater porosity, exhibiting a high double-layer capacitance that is 25 times greater than that of Cu [30]. To make the electrodeposition, a team of three electrodes is used, being FTO with a PS template on its surface as a working electrode, a Cu sheet as a counter electrode and a saturated calomel electrode (SCE) as a reference electrode. Cu_2O is obtained by carrying out the electrochemical reduction of a solution of 3 M lactic acid and 0.4 M $CuSO_4$. The electrochemical deposition is carried out at -0.7 V vs SCE for a period of 20 minutes. To adjust the pH to 12, a 10 % by weight NaOH solution is added. The temperature should be kept constant at 45 °C. Subsequently, the electrode is submerged in tetrahydrofuran to remove the polystyrene template and/or it is calcined up to 500 °C in a N_2 atmosphere with a speed ramp of $2\ °C\ min^{-1}$. Its final morphology can be seen in Fig. 26 [21,64,114].

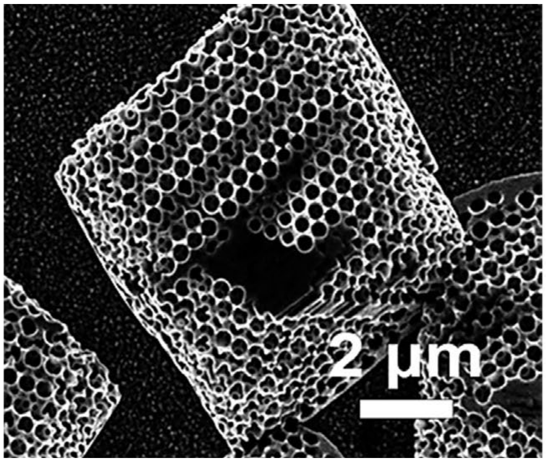

Fig. 26. High magnification SEM image of Cu_2O inverse Opal [21].

J. Mex. Chem. Soc. **2023**, *67*(4)
Special Issue
©2023, Sociedad Química de México
ISSN-e 2594-0317

In electrochemistry Cu_2O is a p-type semiconductor and is used as an electrocatalyst to reduce CO_2 to CO and hydrocarbons (CH_4, C_2H_4, CH_3OH and HCOOH) and also to generate hydrogen. It is also used as a sensor for hydrogen peroxide and glucose. It is widely used in different methods for obtaining carbon-free electricity such as wind, solar, and hydroelectric power, among others [21,64,115]. Table 11 shows how the inverse opal has a large specific capacitance compared with other microstructures.

Table 11. Comparison of the specific capacitance (C_m) of different Cu_2O electrodes with different crystal forms.

Morphology	Method of preparation	C_m(F g^{-1})	Scan rate	References
Microcubes	Hydrothermal	660	1 A g^{-1}	[116]
Inverse opals	electrodeposition	502	10 mV s^{-1}	[116]
Microsphere	Polyol reduction	173.2	5 mV s^{-1}	[117]
Cubes	Polyol reduction	157.5	5 mV s^{-1}	[117]
Microsphere	Polyol reduction	144	0.1 A g^{-1}	[116]
Flower-like	Polyol reduction	92.3	5 mV s^{-1}	[117]

Hematite ($\alpha - Fe_2O_3$)

The iron oxides present polymorphism, being the following phases: hematite ($\alpha - Fe_2O_3$), β phase iron oxide ($\beta - Fe_2O_3$), maguemite ($\gamma - Fe_2O_3$), epsilon phase iron oxide ($\varepsilon - Fe_2O_3$) and magnetite (Fe_3O_4) [118]. Hematite is an n-type semiconductor that can adhere to the surface of a transparent crystalline electrode such as the FTO or ITO allowing incident solar radiation to pass through. $\alpha - Fe_2O_3$ has a bandgap of 2.1 eV making it possible to absorb both a portion of UV radiation and visible light [119,120], as can be seen in Fig. 27.

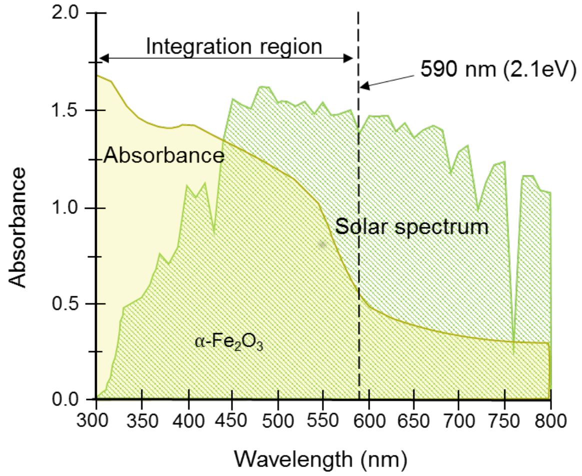

Fig. 27. Solar UV-Vis absorption spectrum of hematite [121].

A theoretical solar to hydrogen conversion efficiency (STH) of 16.8 % (or photocurrent generation of 12.6 mA cm^{-2} at 1.23 V vs. AM 1.5G SHE under irradiation of 1 sun (100 mW cm^{-2}) and an appropriate position of the band energy [18,122,123]. Experimentally, a water breaking efficiency of 13 % has been obtained, resulting in a hydrogen efficiency of 1-2 % [124]. Its photonic bandgap is ~428 nm. It presents different current densities depending on the morphology obtained by the type of synthesis used [35]. In Fig. 28 we see the basic hexagonal structure of hematite; it consists of 30 atoms where Fe^{3+} has a coordination of 6 and O^{2-} works with a coordination of 4. The crystalline planes of α-hematite are: (104), (110), (214), (125) and (128) [118].

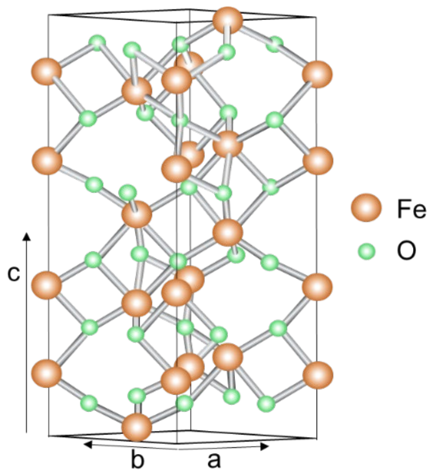

Fig. 28. Crystal structure of $\alpha - Fe_2O_3$ with coordinated lattices (a)-(c) [124].

The cell parameters proposed by Smart TJ 2017 are: a = b = 5.13 Å and c = 13.99 Å with $Fe - O$ bonds of 1.99 and 2.14 Å and $O - Fe - O$ angles = 90.7°, 86.0° and 78.6° [124, 125], with an E_g = 2.2 eV [126] and $\mu_{Fe}(\mu_B)$ of 4.6 [127]. On the other hand, hematite has a low density of charge carriers, as well as low mobility of charge carriers ($<10^{-2}$ cm^2 V^{-1} S^{-1}) and a high rate of recombination of the pair e^-/h^+ [124,128], so it is not very efficient. Shi X., et al. 2013 has mentioned that the geometry of the microstructure with which the hematite is deposited on the FTO or ITO influences the efficiency of the photoelectrode. Among the different morphologies we have nanotubes, nanorods, nanocauliflowers, nanosheets, and inverse opal [119]. As can be seen in table 12, the hematite deposited in the form of cauliflower presents the highest photocurrent density of 3.0 mA cm^{-2}, while the one deposited in the form of nanoparticles presented the lowest photocurrent density of 0.3 mA cm^{-2} [1].

Hematite ($\alpha - Fe_2O_3$) is used as magnetic material, catalysis, pigments, gas sensors, optical and electromagnetic equipment. It is stable under ambient conditions and with high resistance to corrosion, which is why it is used in the conversion of solar energy and in the production of hydrogen and oxygen from the breaking of bonds in the water molecule using a photoelectrochemical cell [119]. Its conversion efficiency from monochromatic incident photon to electron is 19.3 % under 10 times simulated solar illumination [35]. The introduction of defects such as oxygen vacancies (V_O) increase the current density in hematite by donating two electrons to the system. Vacancies behave like n-type semiconductors. Polarons are created near the Fe ion by the presence of ionized electrons from the V_O. As the concentration of V_O increases, the conversion efficiency of the incident photon to current increases, as does the density of the carriers, their mobility and adsorption of visible light. There are two possible explanations for the above behavior: (a) oxygen vacancies increase the conductivity properties of bulk carriers as the internal geometry relaxes in the presence of oxygen or, (b) oxygen vacancies increase the gap between the gap and the electron at the electrode/electrolyte interface [124]. Among the limitations found for the use of hematite must be a short hole diffusion length, high recombination speed of the e^-/h^+ pair, poor charge mobility, poor OER and slow charge transfer kinetics [122]. The OER in hematite is using four electrons (equation 2) and for the HER two electrons are necessary (equation 3) [129].

An example of how to carry out the deposit of hematite in FTO is by means of electrodeposition (Section electrodeposit), for which the FTO is initially submerged in a mixture of acetone and ethanol and shaken with sonication for 20 minutes. Subsequently, the FTO is submerged in a mixture of sulfuric acid liquor and hydrogen peroxide (piranha solution) for 20 minutes to make the surface hydrophilic. Finally, the washed FTO is submerged in the polystyrene colloidal suspension and placed in an oven at 50 ℃ for two days (submersion method). To deposit hematite on the FTO/polystyrene substrate, a solution is first prepared containing 60 g iron sulfate (98 % $FeSO_4 \cdot 7H_2O$), 1.5 g ascorbic acid (99 % $C_6H_8O_6$), 0.5 g of amidosulfonic acid (99 % H_2NSO_3H) and 15 g of boric acid (99 % H_3BO_3) in one liter of distilled water. All this in an electrolytic cell (Fig. 14 **(a)**) composed of three electrodes with FTO/PS as working electrode, a Pt sheet as

J. Mex. Chem. Soc. **2023**, *67*(4)
Special Issue

ISSN-e 2594-0317

counter electrode and Ag/AgCl as reference electrode. A constant potential is applied vs. Ag/AgCl of -0.5 V to the working electrode, in order to control the thickness of the Fe deposit, the run is made for a determined period of time, the time finding that the most appropriate time for the desired thickness is 9 minutes. Finally, an annealing of the electrode obtained at 400 °C provides us with the hematite inverse opal with good photoelectric behavior to carry out different reactions [119,120]. Fig. 29 shows us the micrograph of hematite inverse opal obtained by in situ hydrolysis of ferric ions in low relative humidity [35].

Table 12. Different hematite nanostructures and their performance in photo-electrochemical (PEC).

Morphology	**photocurrent**	**E/V**	**vs.**	**Reference**
Cauliflowers	3.0 mA cm^{-2}	1.23	RHE	[130]
Nanoflowers	0.35 mA cm^{-2}	0.23	Ag/AgCl	[131]
Nanotubes	1.42 mA cm^{-2}	0.5	Ag/AgCl	[132]
Mesopores	0.56 mA cm^{-2}	1.23	RHE	[133]
Nanoparticles	0.30 mA cm^{-2}	1.23	RHE	[134]
Nanospheres	23.6 μA cm^{-2}	1.1	NHE	[135]
Nanopetals	0.39 mA cm^{-2}	1.23	RHE	[136]
Nanoparticles (clustered)	61 μA cm^{-2}	0.23	Ag/AgCl	[137]
Hexagonal	1.6 mA cm^{-2}	0.6	Ag/AgCl	[138]
Nanorods	700 μA cm^{-2}	1.6	RHE	[1]
Nanowires	1.24 mA cm^{-2}	1.23	RHE	[139]
Inverse opal	3.1 mA cm^{-2}	0.5	Ag/AgCl	[119]

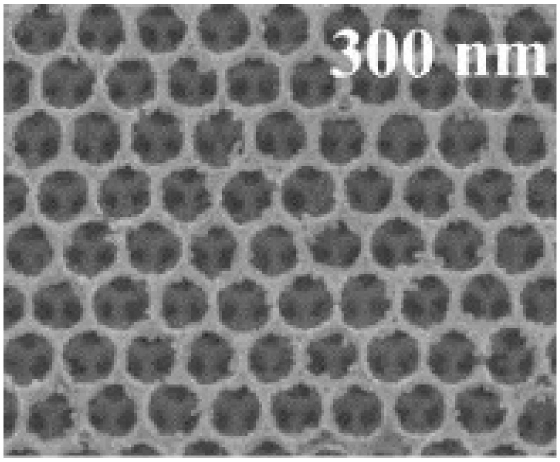

Fig. 29. Hematite inverse opal deposited via in situ hydrolysis of ferric ions at a low relative humidity of 30% [35].

Titanium dioxide (TiO_2)

TiO_2 is an n-type semiconductor with three crystalline structures: anatase (tetragonal), rutile (tetragonal) and brookite (orthorhombic), the first two being used as photoelectrodes. Fig. 30 shows us the crystalline structure of anatase (Fig. 30**(a)**) and rutile (Fig. 30**(b)**). The tetragonal crystal structure of anatase is formed by a chain of distorted TiO_6 octahedrons, resulting in a unit cell containing four Ti atoms at positions (0,0,0), ($\frac{1}{2}$, $\frac{1}{2}$, $\frac{1}{2}$), (0, $\frac{1}{2}$, $\frac{1}{4}$) and ($\frac{1}{2}$,0, $\frac{3}{4}$) and eight oxygen atoms [140]. It has two dominant crystalline structures (101) that adsorb oxygen molecules and benefit the production of superoxide radicals [2]. Rutile has a tetrahedral structure with two titanium atoms and four oxygen atoms per unit cell. The relative positions of titanium in rutile are (0,0,0) and ($\frac{1}{2}$, $\frac{1}{2}$, $\frac{1}{2}$) [141]. Titanium dioxide is environmentally friendly, low cost, high oxidizing power, high rate of recombination of the electron/hole pair, low ability to absorb sunlight [142].

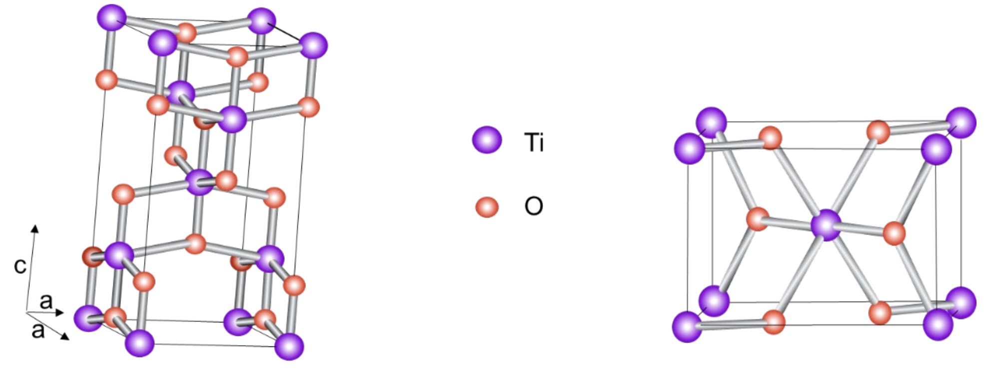

(a) (b)

Fig. 30. (a) Anatase unit cell. The oxygen atoms form a distorted octahedron with a titanium atom in the center [140]. **(b)** Rutile unit cell. The oxygen atoms form an ordered hexagon with half the sites occupied by titanium atoms [141].

The band gap is influenced by the relationship of the valence band of Ti^{4+} with the "2p" orbitals of the oxygen that composes it. The band gap for rutile is 3.0 eV and for anatase 3.2 eV. This bandgap energy allows absorption in the UV region [143], as seen in Fig. 31 [144]. They also present slow transfer of charge carriers [2]. This compound is chemically stable in different chemical environments, resistant to photocorrosion, non-toxic, abundant with good biocompatibility and high photogeneration of oxidizing holes. These compounds are widely used in photoelectrochemical cells for the breakdown of water molecules and the obtaining of hydrogen and oxygen in the gaseous state as they present a favorable band edge position for redox reactions of water [67]. To increase the efficiency in this type of reactions, doping, metallic deposition, and formation of heterostructures have been attempted [142].

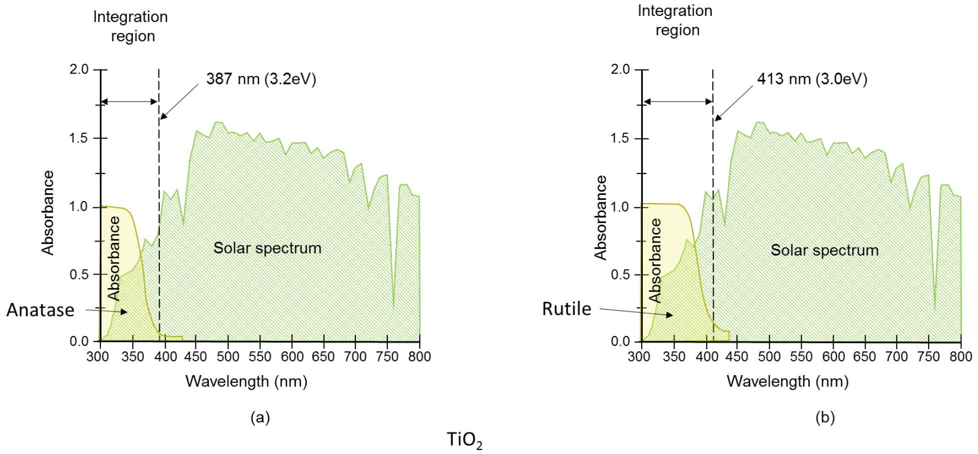

Fig. 31. Solar UV-Vis absorption spectrum of **(a)** Anatase and **(b)** Rutile [144].

J. Mex. Chem. Soc. **2023**, *67*(4)
Special Issue

ISSN-e 2594-0317

For its deposit in the FTO/PS by means of sol gel, 5 mL of titanium isopropoxide are mixed in 47 mL of ethanol with stirring at 1000 rpm. To the mixture is added a mixture of 2 mL of 37 % HCl and 2 mL of deionized water. Mix with stirring for 30 minutes until obtaining transparency and homogeneity. Then 5 drops of the synthesized precursor are added to the FTO/PS. This last operation is repeated 2 more times to increase the electrode filling efficiency. It is dried for 24 hours in the air and finally calcined in air with a ramp of 2 ℃ min^{-1} up to 500 ℃, keeping it at that temperature for 3 hours. The inverse opal can be seen in Fig. 32 [67,143]. Table 13 shows how the capacitance depends of different structures of TiO_2 and preparation method.

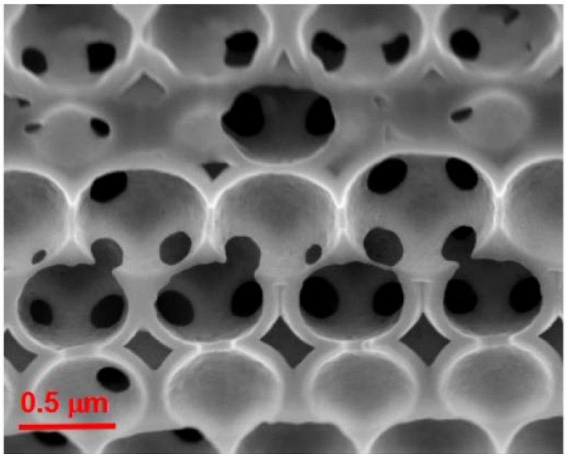

Fig. 32. SEM image of inverse opal cross section of TiO_2 [143].

Table 13. Comparison of the specific capacitance (C_m) of different TiO_2 electrodes with different crystal forms.

Morphology	Method of preparation	$C_m(F\ g^{-1})$	Scan rate	References
Nanoporous	Solvothermal	93.2	$0.5\ A\ g^{-1}$	[145]
Nanofiber	Electrospinning annealed	65.84	$1\ mV\ s^{-1}$	[146]
Nanotubes	Anodic oxidation	19.2	$1\ mV\ s^{-1}$	[147]
Nanoparticles	Microwave power	12		[148]
Nanofiber	Electrospinning annealed	11.33	$2\ V\ s^{-1}$	[146]

Nickel oxide (NiO)

Nickel oxide (bunsenite) is dark green in colour [149]. It is a p-type semiconductor with a band gap between 3.6 and 3.8 eV and covers a small portion of the solar spectrum (Fig. 33).

J. Mex. Chem. Soc. **2023**, 67(4)
Special Issue

ISSN-e 2594-0317

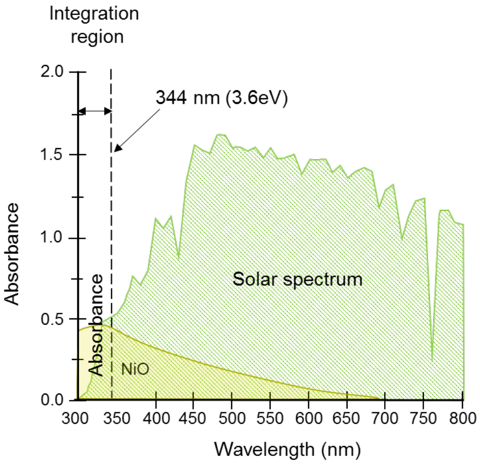

Fig. 33. Solar UV-Vis absorption spectrum of NiO [150].

Among its applications are alkaline batteries, electrochemical capacitors, electrochromic equipment [150,151], energy storage, optoelectronic equipment, ink-sensitive cathodic solar cells and breakdown of the water molecule. NiO falls into Mott-Hubbard type insulators caused by a Coulomb repulsion between 3d electrons and a charge transfer semiconductor. It has good mechanical stability, strong adhesion to transparent semiconductors, and excellent photoelectrochemical properties at thicknesses between 0.2 < 1 < 3.5 µm. Thin films of NiO (< 3.0 µm) and $\mathrm{Ni(OH)_2}$, which is the $\mathrm{Ni^{2+}}$ ion, present a transparent color in the visible spectrum [152] while NiOOH and $\mathrm{Ni_2O_3}$ that have a $\mathrm{Ni^{3+}}$ ion, have a brown coloration [153]. NiO is used as a p-type TCO being used as display equipment, chemical sensor layer, in transparent electronic equipment and magnetic properties in nanoparticles [154]. In the presentation of transparent film it is used as an anode in industrial electrolytic plants for the decomposition of water. NiO has two crystalline structures; for $\beta-\mathrm{NiO}$ is the face-centered cubic with a cell parameter value of a = 4.1769 Å (Fig. 34**(a)**) [149,153], whose diffraction peaks in XRD are (1 1 1), (2 0 0), (2 2 0), (3 1 1) and (2 2 2). The $\alpha-\mathrm{NiO}$ in the hexagonal phase (Fig. 34**(b)**) has the diffraction peaks at (0 0 1), (1 0 0), (1 0 1), (1 0 2), (1 1 0) (1 1 1), (1 0 3) and (2 0 1) and whose cell constants have a size of a = 3.126 Å , b = 3.125 Å and c = 4.605 Å and presenting an angle of 120° between their walls. [155].

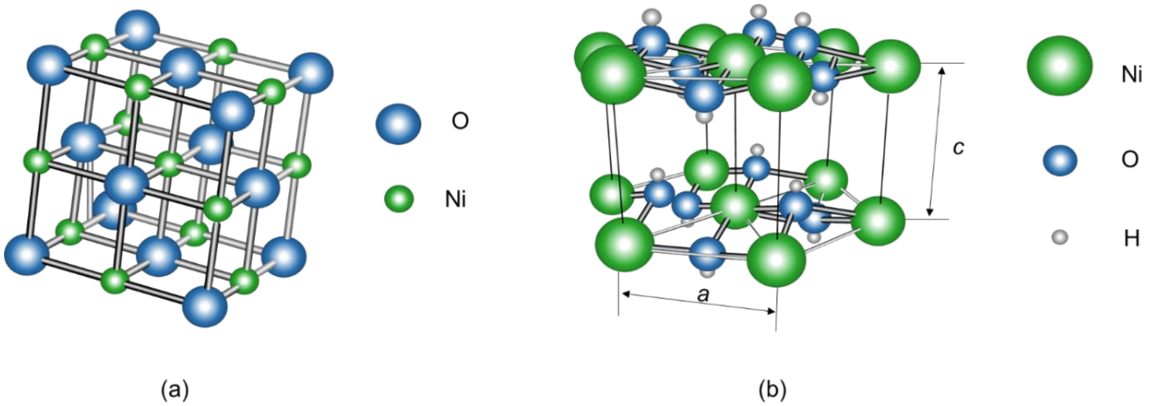

Fig. 34. (a) Crystalline arrangement of $\beta-\mathrm{NiO}$ and **(b)** $\alpha-\mathrm{NiO}$ [153].

J. Mex. Chem. Soc. **2023**, *67*(4)
Special Issue
©2023, Sociedad Química de México
ISSN-e 2594-0317

The synthesis methods of this type of photoelectrodes have been dripping, chemical precipitation, hydrothermal, sol-gel, and electrochemical deposition. With electrochemical deposition it is possible to control the thickness, the composition of the layer and the crystalline morphology, controlling variables such as the composition of the solution, temperature, and the potential or current applied. NiO is prepared by cathodic electrodeposition using a polar aprotic solvent such as dimethyl sulfoxide (DMSO) using a low overpotential. In a three-electrode electrochemical system like the one shown in Fig. 14**(a)**, with FTO/PS as the working electrode, a Pt foil as the counter electrode, and a saturated calomel reference electrode. A solution containing 0.2 M nickel nitrate hexahydrate $[Ni[NO_3]_2 \cdot 6H_2O]$ in DMSO is prepared and the mixture is poured into a vial to be bubbled with Ar. The container is stoppered and heated to 90℃ in a water bath. Before making the deposit, the solution is shaken for 2 minutes. During electrodeposition, the mixture is heated to 80 °C with magnetic stirring at 250 rpm and an overpotential of -0.85 V vs. standard calomel electrode for 250 seconds. Finally, the polystyrene template was removed by heat treatment at 200 °C for 10 min, finally obtaining the desired inverse opal (Fig. 35) [151].

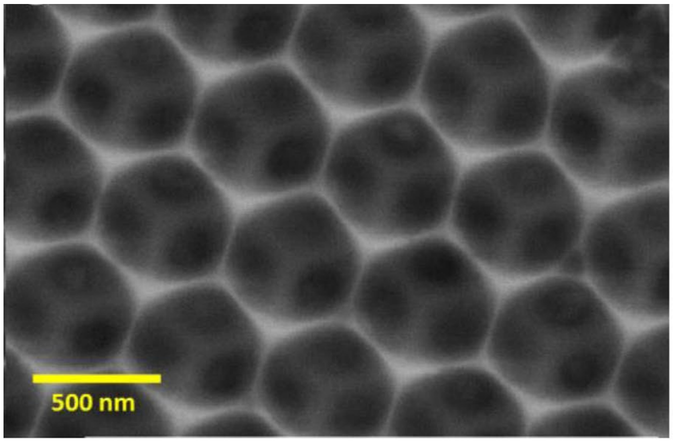

Fig. 35. SEM image of electrodeposited NiO inverse opal macroporous layer [151].

Breakdown reactions of the water molecule in different substrates by photoelectrochemistry

Titanium dioxide (TiO_2)

The typical water breakdown process by the photoelectrocatalytic method in TiO_2 consists of the hydrogen evolution reaction and the oxygen evolution reaction, as shown in Fig. 36. It can be seen that when irradiating TiO_2, thermodynamically the energy level of the conduction band is more negative than the energy level for the production of hydrogen by reducing protons from the water molecule and producing H_2 (H^+/H_2O, 0V vs NHE). The valence band energy level is more positive than the oxidation level of water causing the holes created to oxidize water to form O_2 (H_2O/O_2, 1.23V vs NHE). Applying an overpotential to the counter electrode favors this reaction and thus decreases the recombination of the e^-/h^+ pair [2]. The reactions that occur are:

$$4TiO_2 + 4h\nu \rightarrow 4e^- + 4h^+ \quad (1)$$

Oxidation $$2H_2O + 4h^+ \rightarrow O_2 + 4H^+ \quad (2)$$

Reduction $$4H^+ + 4e^- \rightarrow 2H_2 \quad (3)$$

Total reaction $$2H_2O \rightarrow 2H_2 + O_2 \quad (4)$$

Where *h* is Planck constant and ν frequency.

Fig. 36 represents the photocatalytic method **(a)** or the photoelectrochemical method **(b)** to produce H_2. In Fig. 36**(b)** we can see that the photoelectrochemical method has a photoelectrode that is connected to a source to have

J. Mex. Chem. Soc. **2023**, *67*(4)
Special Issue

ISSN-e 2594-0317

an overpotential. Similarly, when TiO_2 is irradiated with light, valence band electrons are excited to move to the conduction band, leaving holes in the valence band. The electrons move in an external electrical circuit until they reach the counter-electrode, where the protons are reduced to H_2. At the same time, the holes oxidize water molecules to generate oxygen (or can be used to generate $^{\cdot}OH$ radicals, useful in degrading contaminants in solution) [2]. In Fig. 37 we observe the kinetic behaviour when using a TiO_2 working photoelectrode, a Pt counter electrode and an Ag/AgCl (3M KCl) reference electrode. The flat band potential V_{fb} = -0.16 V at pH = 0 vs NHE. Obtained from: V_{fb} = (-0.17 ± 0.02) – 0.054 (pH) V vs NHE, measured in three different HCl solutions (0.1 M; pH 1.1); NaCl (0.1 M; pH 6.9) and NaOH (0.1 M; pH 12.3). The applied overpotential is 0.5 V vs Ag/AgCl. The value of V_{fb} is fused with the edge of the minimum conduction band allowing the reduction of water [153]. The conduction band potential of anatase is E_C = -0.1 V and the valence band potential is E_V = 3.1 V at pH = 0 vs NHE [156].

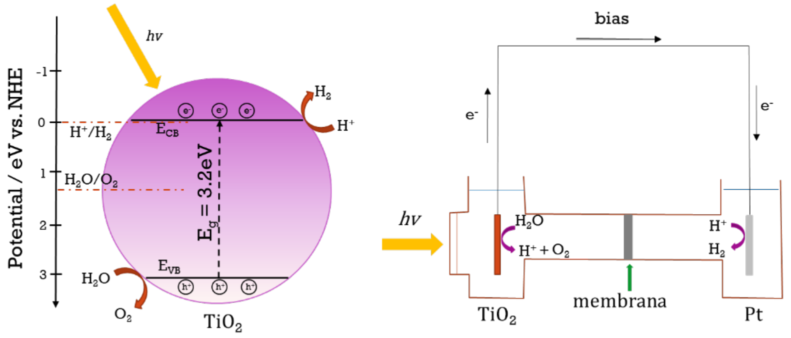

(a) (b)

Fig. 36. (a) Electrons in the conduction band that reduce protons to hydrogen and holes in the valence band oxidize water to produce oxygen or widely used in different methods for obtaining widely used in different methods for obtaining $^{\cdot}OH$ radicals (not shown) to degrade pollutants E_C = -0.1 V and E_V = 3.1 V at pH = 0 vs. NHE. **(b)** Holes in the TiO_2 surface react with water to generate oxygen and hydrogen ions. Electrons in the counter electrode react with hydrogen ions to generate hydrogen [2,156].

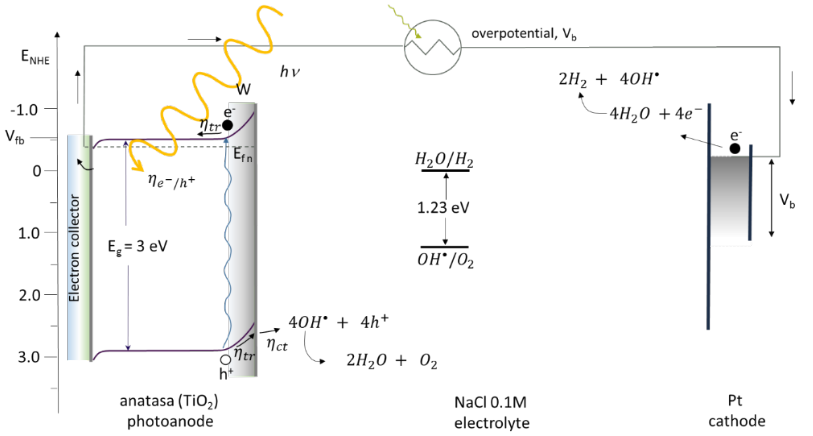

Fig. 37. Energy diagram showing a typical value of the flag band potential, V_{fb}, of n-type hematite, in the photoelectrochemical cell the water-breaking operation is aided by solar illumination and an applied external overpotential to the system, V_b. W is the thickness of the charge or depletion space, E_g is the bandgap energy, η_{e^-/h^+} light absorption, η_{tr} charge transport, η_{ct} chemical reactions at the surface, E_{fn} Fermi energy of n-type photoelectrode [157–159].

J. Mex. Chem. Soc. **2023**, *67*(4)
Special Issue

ISSN-e 2594-0317

Nickel oxide (NiO)

Nickel oxide is used in alkaline conditions due to its low cost, high catalytic activity and corrosion stability [3]. The breakdown of the water molecule proceeds via coordination with Ni (II) centers on the surface. This causes the NiO to dissolve causing changes in the oxidation state of Ni to values >2. Anodic polarization of NiO in neutral aqueous solution creates polymorphic oxohydroxide species (NiOOH) with Ni ions on the deposit surface (Fig. 38). The different polymorphic structures are probably due to the irregular geometry of the coordinated Ni centers on the surface. These forms are: $\beta-\mathrm{NiOOH}$ which has a valence band of +3 or slightly lower for the Ni ion, due to the presence of small amounts of $\mathrm{Ni(OH)_2}$. In $\gamma-\mathrm{NiOOH}$, nickel has a valence between 3.5-3.7 and its stoichiometry is 0.835 $\mathrm{NiO_2}$- 0.165 $\mathrm{Ni(OH)_2}$ where the presence of $\mathrm{Ni^{4+}}$ and $\mathrm{Ni^{2+}}$ is seen. For the catalytic formation of $\mathrm{O_2}$ there is the intermediate $\mathrm{NiOO_2}$ that contains $\mathrm{Ni^{2+}}$. Oxidation reactions occur over a range of potentials. At lower potential the oxidation reaction from Ni (II) to Ni (III) is:

$$\mathrm{NiO(OH)_n(H_2O)_p \rightarrow NiO(OH)_{n+1}(H_2O)_{p-1} + e^- + H^+} \tag{5}$$

At higher potentials oxidation of Ni (II) to Ni (III) can occur

$$\mathrm{NiO(OH)_{n+1}(H_2O)_{p-1} \rightarrow NiO(OH)_{n+2}(H_2O)_{p-2} + e^- + H^+} \tag{6}$$

or the oxidation of Ni (III) to Ni (IV)

$$\mathrm{NiOO(OH)_{m-1} \rightarrow NiOO_2(OH)_{m-2} + e^- + H^+} \tag{7}$$

The equations (6) and (7) show that the oxidative process of NiO is compensated by the removal of a proton from the hydroxyl group coordinated with the Ni centers on the surface. In addition to this, the coordination surface between the hydroxyl group and the Ni centers is more regular, allowing obtaining valences greater than 2 [152]. Fig. 39 shows that NiO is a p-type semiconductor with a band gap between 3.15 and 3.8 eV [160] and a Fermi energy of -0.955 eV [161]. The conduction band has a value of -0.5 V and the valence band of 2.93 V [97]. For the hydrogen evolution reaction, it is observed how a two-step process is involved on the surface of the NiO electrode, first the Volmer reaction:

$$\mathrm{H_2O + e^- \rightarrow H^* + OH^-} \tag{8}$$

associated with hydrogen adsorbed in the photoelectrocatalysis on the electrode. The second step is the Heyrovsky reaction:

$$\mathrm{H^* + H_2O + e^- \rightarrow H_2 + OH^-} \tag{9}$$

or the Tafel reaction [101, 162]:

$$\mathrm{H^* + H^* \rightarrow H_2} \tag{10}$$

In the same way on the Pt electrode the oxygen evolution reaction occurs from either the dissociation of the water molecule to form the hydroxide ion, or from the hydroxide that is in the middle, being the hydroxide ion adsorbed on the electrode surface. By combining the electrons of the adsorbed hydroxide and the photogenerated holes, the electrical circuit is closed. The adsorbed hydroxide combines with other adsorbed hydroxide molecules, forming peroxide on the surface, which finally combines with itself to form adsorbed oxygen [163].

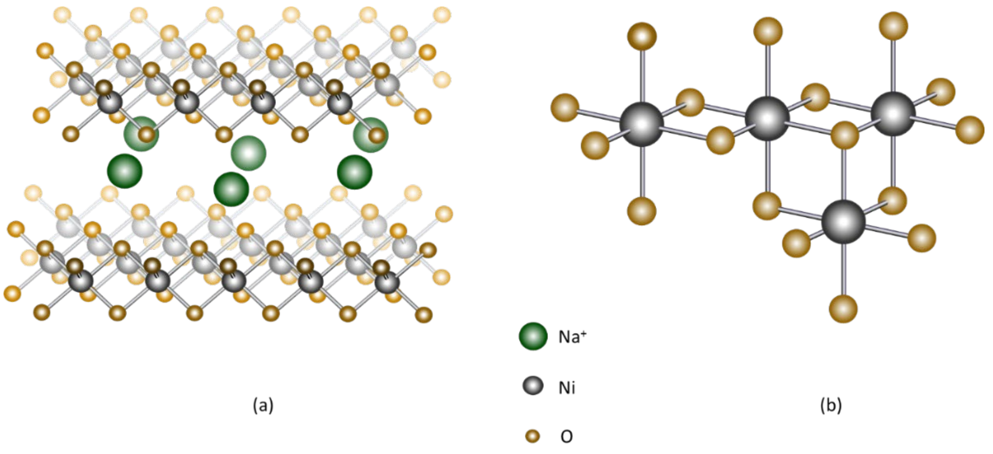

Fig. 38. (a) X-rays of the crystal structure of $\gamma-$ NiOOH showing nickel in gray, oxygen in orange, and sodium ions in green. The sodium ion is the alkaline cation added to the solution and combines with the water molecules at the NiO_6 boundary with the $\gamma-$ NiOOH. The water molecules are sandwiched between the NiO_2 slabs. **(b)** Fragment of the NiO_6 octahedron structure [3].

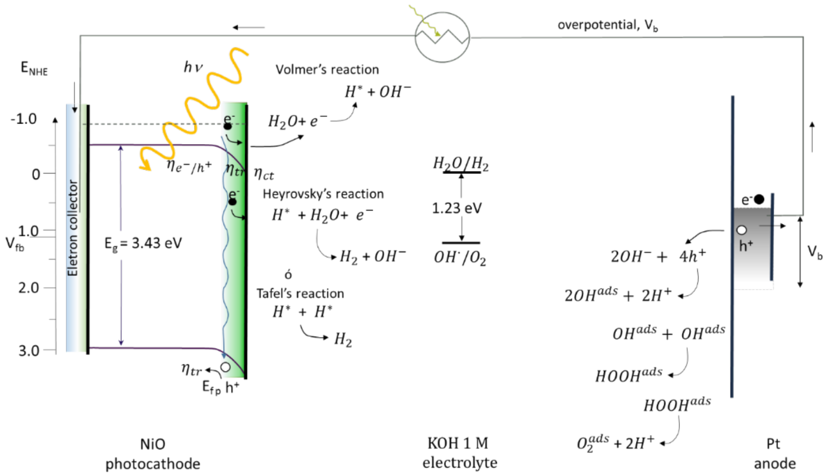

Fig. 39. Photoelectrochemical cell with NiO working electrode, Pt auxiliary electrode and Ag/AgCl reference electrode, and 0.1 M NaOH supporting electrolyte [161].

Hematite ($\alpha-Fe_2O_3$)

Hematite has a small bandgap (2.1 eV), which means that it can absorb light with wavelengths above 400 nm [1], but at the same time makes it necessary to add an external potential to complete the rupture reaction of the water molecule. Fig. 40 shows a flat band potential at very low energy ($V_{fb} = 0.4$ V vs RHE [164]) for water reduction. Following the described reactions, the h^+ produced reacts with the $^{\cdot}OH$ radical oxidizing oxygen and later form O_2. With the help of the applied overpotential the water molecule provides the H^+ and reduces it to H_2 at the cathode by the electron formed in the hematite photoanode. This reaction is carried out in a three-electrode system having a hematite photoelectrode, a Pt vs. RHE and in 1 M NaOH solution [132,164]. The efficiency that it presents for the breakdown of the water molecule is 13 % [1].

J. Mex. Chem. Soc. **2023**, *67*(4)
Special Issue

ISSN-e 2594-0317

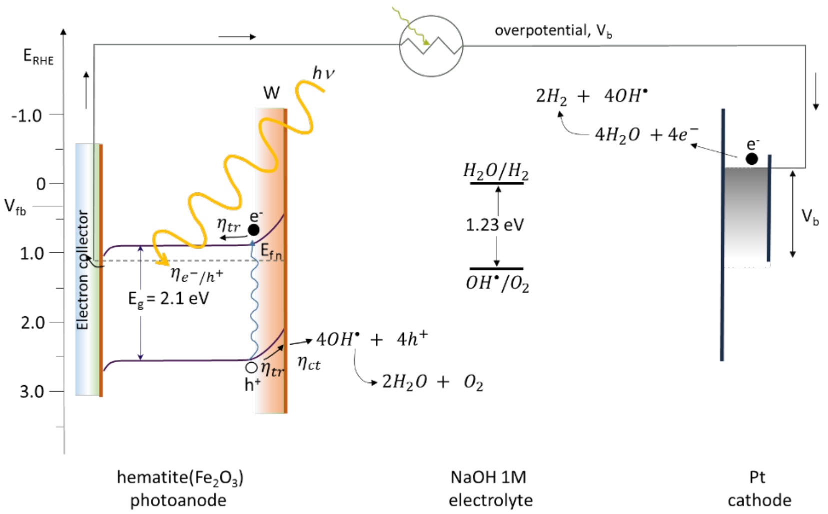

Fig. 40. Energy diagram showing a typical value of the flag band potential, V_{fb}, of n-type hematite, in the photoelectrochemical cell the water-breaking operation is aided by solar illumination and an applied external overpotential to the system, V_b. W is the thickness of the charge or depletion space, E_g is the bandgap energy, η_{e^-/h^+} light absorption, η_{tr} charge transport, η_{ct} chemical reactions at the surface, E_{fn} Fermi energy of type photoelectrode *n* [164–166].

Zinc oxide (ZnO)

ZnO is an n-type semiconductor. Fig. 41 shows that it has a forbidden band of 3.215 eV, valence band is 3.090 eV, conduction band -0.254 eV, flat band potential -0.254 eV (vs NHE) [167]. When this electrode is irradiated, the electrons first form in the conduction band, then they move to the valence band and from there they move to the conductive side of the substrate. From there, its movement is along the external circuit of the system, reaching the counter electrode, enriching it with electrons. Finally, the electrons cause electrochemical reactions that decrease the speed of recombination and reduce the water molecule with the help of an external potential (As can be seen in the following equation) producing hydrogen [71]. The electrons are trapped by the vacancies caused by the desorption of oxygen, increasing both the charge density and the oxidation reaction of water [74]. On the other hand, the holes that are generated in the valence band and that are found in the photoelectrode are captured inside the electrolyte by the electrons of the water, causing its oxidation (equation 1) [4]. In alkaline pH, the $\mathrm{OH}'\mathrm{s}$ are adsorbed on the electrode surface to receive the photogenerated holes [17]. The general reaction to obtain H_2 from this type of electrodes is:

$$4h\nu_0 + (\mathrm{n-semiconductor}) + 2H_2O \rightarrow H_2 + O_2 + (\mathrm{n-semiconductor}) \quad (11)$$

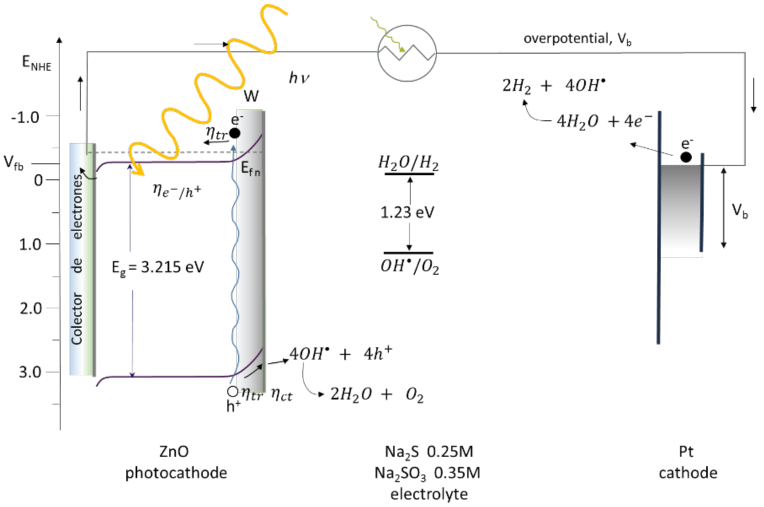

Fig. 41. Breaking of the water molecule using ZnO as working electrode, Pt counter electrode, Na_2SO_3 (0.35 M) and Na_2S (0.25 M) solution [167].

Nickel sulfide (NiS)

Nickel sulfides hold promise for electrolysis in the HER and for their long operational stability in acidic and alkaline solutions. Fig. 42 represents a photoelectrochemical cell with a NiS photoelectrode and a platinum auxiliary electrode working in acid medium. Thus using an pH 0 solution (0.5 M H_2SO_4) the reaction is carried out with an overpotential of 0.215 V, sweep speed of 2 mV s^{-1} and a delivered current density of 10 mA cm^{-2} (vs. RHE) with and flat band potential (V_{fb}) of 1.14 eV (vs NHE). Through the Volmer reaction and later the Heyrovsky or Tafel reaction, the S anion acts as an active site for the adsorption of H^+ and promotes the reduction to H_2. The sulfur atom is the most anionic atom in the NiS crystal lattice. The Ni cation contributes to increase the kinetics of H_2 evolution.

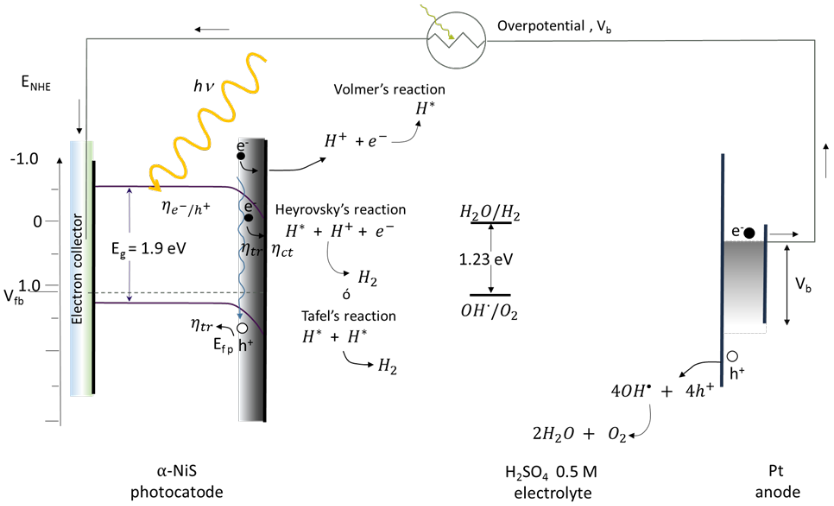

Fig. 42. Water cleavage reactions using an ITO/ NiS photoelectrode in an acid medium. The flat band potential of NiS is E_{fb} = 1.14 V, conduction band potential E_{CB} = -0.66 V, valence band potential E_{VB} = 1.24 (vs NHE), and bandgap energy E_g = 1.9 eV. 300 W Xe lamp illumination [101,162,168].

J. Mex. Chem. Soc. **2023**, *67*(4)
Special Issue
©2023, Sociedad Química de México
ISSN-e 2594-0317

In an alkaline medium (1 M KOH, pH 14) at an overpotential of 0.256 V at a sweep rate of 2 mV s^{-1} and a current density of 10 $mA \cdot cm^{-2}$, the Ni cation adsorbs water and promotes its dissociation, the H^* formed moves to the adjacent anionic atom S and reduces H^+ to produce H_2. Initially the Volmer reaction occurs and subsequently the Heyrovsky or Tafel reaction (reactions shown in section 5.2). Finally, the H^* formed from the dissociation of water moves to the adjacent anionic S atom which reduces to H_2 [101,162]. The proposed reactions can be seen in Fig. 43. Thus, we have that $\alpha - NiS$ generates 13.413 mmol h^{-1} g^{-1} of H_2 with a conversion efficiency of 5.2 %, while $\beta - NiS$ generates 12.731 mmol $\cdot$ h^{-1} g^{-1} of H_2 and its conversion efficiency is 4.8 %. Both compounds can be used as sacrificial agents Na_2S and Na_2SO_3 [98].

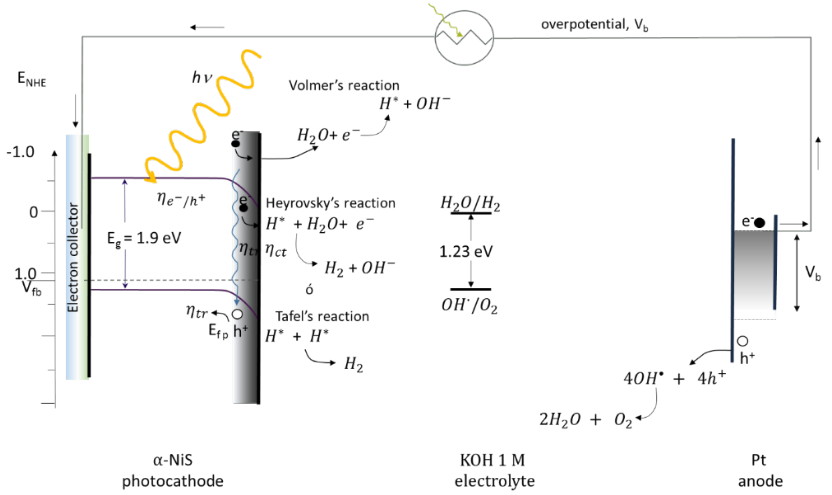

Fig. 43. Water cleavage reactions using an ITO/NiS photoelectrode in alkaline medium. Experiment carried out under the same conditions as in Fig. 42 [101,162,168].

For the oxygen evolution reaction (0.1 M KOH, pH 14), overpotential of 0.384 V, and current density 10 $mA\ cm^{-2}$ (vs RHE) have been used, the reactions in an alkaline medium proposed are:

$$4OH^- \rightarrow O_2 + 2H_2O. + 4e^- \tag{12}$$

Subsequently you have to:

$$OH^- \rightarrow OH^* + e^- \tag{13}$$
$$OH^* \rightarrow O^* + H^* + e^- \tag{14}$$

Followed by:

$$2O^* \rightarrow OR_2 \tag{15}$$

Either

$$O^* + OH^- \rightarrow {}^*OOH + e^- \tag{16}$$
$${}^*OOH + OH^- \rightarrow O_2 + H_2O + e^- \tag{17}$$

*OOH produces NiOOH on the electrode surface.

In this sequence of reactions, the flat band potential for NiS is E_{fb} = 0.4 eV [162]. In Fig. 44 it can be seen how the energy potential of the conduction band (E_{CB}) is above the evolution potential of hydrogen for the

J. Mex. Chem. Soc. 2023, 67(4)
Special Issue

ISSN-e 2594-0317

rupture of the water molecule. Protons are reduced to H_2 by conduction band electrons [98]. But it can be clearly seen that additional energy is required to efficiently reach the OER, so photoelectrochemistry is very useful with this material.

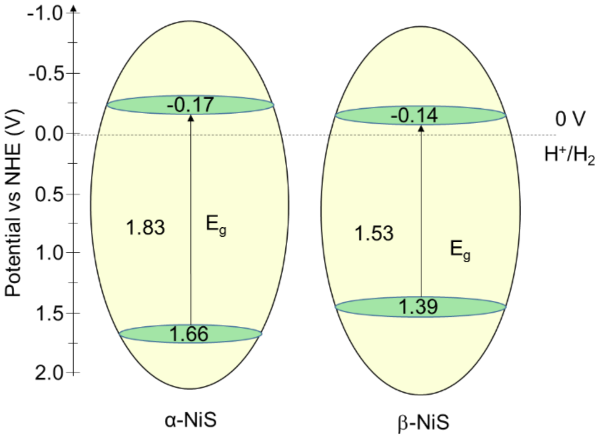

Fig. 44. Band structure of α − NiS and β − NiS [98].

Copper (I) oxide (Cu_2O)

In the process of breaking the water molecule, the photoelectrode with Cu_2O deposit, a *p*-type electrode, has more negative conduction band potential than the reduction potential of hydrogen [169] and the valence band has a lower potential than the evolution potential of oxygen. The photoelectrons will contribute to the formation of hydrogen and the holes will be transferred to the counter electrode to produce oxygen [170]. When Cu_2O is highly active, it presents a photocurrent of up to -7.6 mA cm^{-2} producing 75 ± 10 µL of H_2 at a total charge of 0.58 C at 0 V vs RHE [169]. In Fig. 45 we see the energy diagram for the rupture of the water molecule. The flat valence and conduction energy band of Cu_2O are E_{fv} = 0.64 V and E_{fc} = -1.83 V [156], its flat band potential is V_{fb} = 0.55 V vs RHE [171]. With Pt as the counter electrode, water requires 1.4 to 1.8 V of overpotential for its molecular breakdown. The difference between these values will be reduced depending on the type of photoelectrode and the amount of solar energy reaching the surface [172]. The photogenerated electrons in the Cu_2O will react producing hydrogen from the water, and the holes will move to the counter electrode to carry out the oxygen evolution reaction [170].

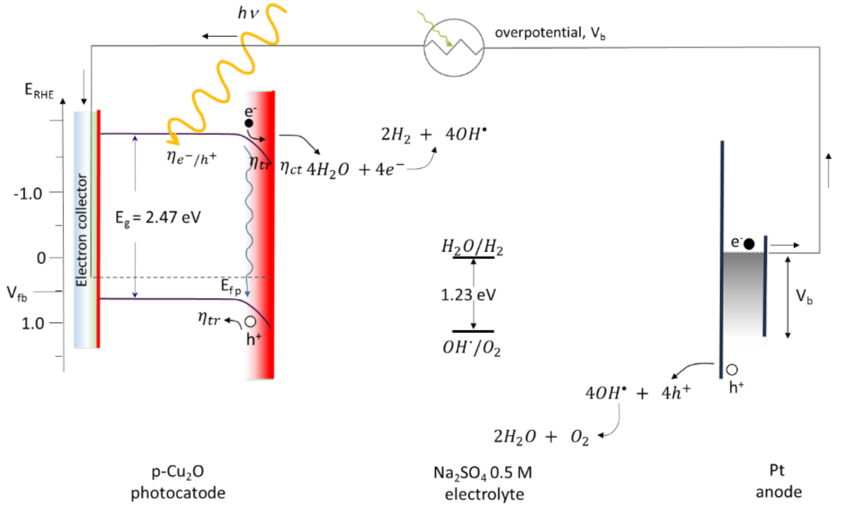

Fig. 45. Energy diagram of *p*-type photoelectrode (Cu_2O) for water molecule cleavage [170,171,173].

J. Mex. Chem. Soc. **2023**, *67*(4)
Special Issue

ISSN-e 2594-0317

Conclusions

Considering the importance of the structure of the binary oxides semiconductors deposited in transparent conductive electrodes used in photoelectrochemistry is essential for the optimization of the process. By increasing the contact surface, the capture of photons increases and with it the efficiency in the conversion of water to hydrogen by this method. Therefore, inverse opal deposits present a very promising alternative to achieve this objective in a controlled and reproducible manner. In this article, the different methods to achieve this mesoporous structure have been reviewed and the semiconductors used in electrodes of photoelectrochemical cells, particularly focused on the water-splitting reaction, have been included. It is essential to continue studying the characteristics of photoactive surfaces and to continue the development of semiconductor deposition methods to obtain controlled, uniform, ordered and highly efficient interfaces. These investigations will help accelerate the transition from fossil fuels to other energy sources for human activities, allowing coexistence with the environment and reducing CO_2 emissions, thus contributing to minimizing the climate change that we have been experiencing in recent decades.

Acknowledgements

The support of CONACYT, through the project A1-S-18230 and PAPIIT-DGAPA UNAM IV200222 are recognized. The technical support of Citlalit Martínez and Dr. Alejandra Pérez Nava are highly appreciated.

References

1. Rahman, G.; Najaf, Z.; Shah, A. ul H. A.; Mian, S. A. *Optik (Stuttg).* **2020**, *200*, 163454.DOI: https://doi.org/10.1016/j.ijleo.2019.163454.
2. Ge, M.; Cai, J.; Iocozzia, J.; Cao, C.; Huang, J.; Zhang, X.; Shen, J.; Wang, S.; Zhang, S.; Zhang, K. Q.; Lai, Y.; Lin, Z. *Int. J. Hydrogen Energy.* **2017**, *42*, 8418–8449. DOI: https://doi.org/10.1016/J.IJHYDENE.2016.12.052.
3. Bediako, D. K.; Lassalle-Kaiser, B.; Surendranath, Y.; Yano, J.; Yachandra, V. K.; Nocera, D. G. *J. Am. Chem. Soc.* **2012**, *134,* 6801-6809. DOI: https://doi.org/10.1021/ja301018q.
4. Sharma, A.; Chakraborty, M.; Thangavel, R.; Udayabhanu, G. *J. Solgel Sci. Technol.* **2018**, *85*, 1–11. DOI: https://doi.org/10.1007/s10971-017-4536-3.
5. Jain, I. P. *Int. J. Hydrogen Energy.* **2009**, *34*, 7368–7378. DOI: https://doi.org/10.1016/j.ijhydene.2009.05.093.
6. Walter, M. G.; Warren, E. L.; McKone, J. R.; Boettcher, S. W.; Mi, Q.; Santori, E. A.; Lewis, N. S. *Chem. Rev.* **2010**, *110*, 6446–6473. DOI: https://doi.org/10.1021/cr1002326.
7. Crabtree, G. W.; Lewis, N. S. In: *AIP Conference Proceedings* 2008, Berkeley, CA, March 1-2, **2008**; *1044*, 309–321. https://doi.org/10.1063/1.2993729.
8. Nikolaidis, P.; Poullikkas, A. *Renewable and Sustainable Energy Rev*. **2017,** *1*, 597–611. DOI: https://doi.org/10.1016/j.rser.2016.09.044.
9. Kudo, A.; Miseki, Y. *Chem. Soc. Rev.* **2009**, *38*, 253–278. DOI: https://doi.org/10.1039/b800489g.
10. Tachibana, Y.; Vayssieres, L.; Durrant, J. R. *Nat. Photonics*. **2012**, *6*, 511–518. https://doi.org/10.1038/nphoton.2012.175.

J. Mex. Chem. Soc. **2023**, *67*(4)
Special Issue
©2023, Sociedad Química de México
ISSN-e 2594-0317

11. Ameta, R.; Solanki, M. S.; Benjamin, S.; Ameta, S. C. Photocatalysis. In: *Advanced Oxidation Processes for Wastewater Treatment: Emerging Green Chemical Technology*; Ameta S., Ameta R., Ed.; Academic Press, **2018**; 135–175. DOI: https://doi.org/10.1016/B978-0-12-810499-6.00006-1.
12. Takanabe, K. *ACS Catal.* **2017**, *7*, 8006–8022. DOI: https://doi.org/10.1021/acscatal.7b02662.
13. Thorne, J. E.; Li, S.; Du, C.; Qin, G.; Wang, D. *J. Phys. Chem. Letters.* **2015**, *6*, 4083–4088. DOI: https://doi.org/10.1021/acs.jpclett.5b01372.
14. Bockris, J. O.; Uosaki, K. *J. Electrochem. Soc.* **1977**, *124*, 98–99. DOI: https://doi.org/10.1149/1.2133256.
15. Cao, S.; Piao, L. *Angew. Chem., Int. Ed. Engl.* **2020**, *59*, 18312–18320. DOI: https://doi.org/10.1002/anie.202009633.
16. Jiang, X.; Lin, Q.; Zhang, M.; He, G.; Sun, Z. *Nanoscale Res. Lett.* **2015**, *10*. DOI: https://doi.org/10.1186/s11671-015-0755-0.
17. Liu, M.; Nam, C. Y.; Black, C. T.; Kamcev, J.; Zhang, L. *J. Phys. Chem. C.* **2013**, *117*, 13396–13402. DOI: https://doi.org/10.1021/jp404032p..
18. Young Kim, J.; Magesh, G.; Hyun Youn, D.; Jang, J.-W.; Kubota, J.; Domen, K.; Sung Lee, J. *Sci. Rep*. **2013,** *3*, 2681. DOI: https://doi.org/10.1038/srep02681.
19. Marlow, F.; Muldarisnur; Sharifi, P.; Brinkmann, R.; Mendive, C. *Angew. Chem., Int. Ed. Engl.* **2009**, *48*, 6212–6233. DOI: https://doi.org/10.1002/ANIE.200900210.
20. Fathi, F.; Rashidi, M. R.; Pakchin, P. S.; Ahmadi-Kandjani, S.; Nikniazi, A. *Talanta.* **2020**, *221*, 121615. DOI: https://doi.org/10.1016/J.TALANTA.2020.121615.
21. Zheng, X.; Han, J.; Fu, Y.; Deng, Y.; Liu, Y.; Yang, Y.; Wang, T.; Zhang, L. Highly *Nano Energy.* **2018**, *48*, 93–100. DOI: https://doi.org/10.1016/J.NANOEN.2018.03.023.
22. Zhou, Y.; Antonietti, M. *Chem. Commun.* **2003**, *3*, 2564–2565. DOI: https://doi.org/10.1039/b307444g.
23. Zhang, L.; D'Acunzi, M.; Kappl, M.; Auernhammer, G. K.; Vollmer, D.; Van Kats, C. M.; Van Blaaderen, A. *Langmuir*. **2009**, *25*, 2711–2717. DOI: https://doi.org/10.1021/la803546r.
24. Ghimire, P. P.; Jaroniec, M. *J. Colloid Interface Sci.* **2020**, *584*, 838–865. DOI: https://doi.org/10.1016/j.jcis.2020.10.014.
25. Waterhouse, G. I. N.; Chen, W. T.; Chan, A.; Sun-Waterhouse, D. *ACS Omega.* **2018**, *3*, 9658–9674. DOI: https://doi.org/10.1021/ACSOMEGA.8B01334/SUPPL_FILE/AO8B01334_SI_001.PDF.
26. Chen, X.; Zhang, Y.; Pang, Y.; Jiang, Q. *Materials.* **2020**, *13*, 1–10. DOI: https://doi.org/10.3390/ma13204647.
27. Zhang, K.; Shi, X.; Kim, J. K.; Lee, J. S.; Park, J. H. *Nanoscale.* **2012**, *5*, 1939-1944. DOI: https://doi.org/10.1039/c2nr33036a.
28. Nishijima, Y.; Ueno, K.; Juodkazis, S.; Mizeikis, V.; Misawa, H.; Tanimura, T.; Maeda, K. *Opt Express.* **2007**, *15*, 12979-12988. DOI: https://doi.org/10.1364/oe.15.012979.
29. Chung, W. A.; Hung, P. S.; Wu, C. J.; Guo, W. Q.; Wu, P. W. *J. Alloys Compd.* **2021**, *886*, 161243. DOI: https://doi.org/10.1016/J.JALLCOM.2021.161243.
30. Zhou, Y.; Zhao, J.; Liu, Y.; Ng, R. J. H.; Yang, J. K. W. *Mater. Sci. Semicond. Process*. **2021**, *121*, 1-8 https://doi.org/10.1016/j.mssp.2020.105444.
31. Sordello, F.; Maurino, V.; Minero, C. *J. Mater. Chem.* **2011**, *21*, 19144–19152. DOI: https://doi.org/10.1039/c1jm12674a.
32. Cho, T.-Y.; Han, C.-W.; Jun, Y.; Yoon, S.-G. *Sci. Rep.* **2013**, *3*, 1496, 1-7. DOI: https://doi.org/10.1038/srep01496.
33. Trang Pham, T. T.; Bessho, T.; Mathews, N.; Zakeeruddin, S. M.; Lam, Y. M.; Mhaisalkar, S.; Grätzel, M. *J. Mater. Chem.* **2012**, *22*, 16201-16204. DOI: https://doi.org/10.1039/c2jm32401f.

J. Mex. Chem. Soc. **2023**, *67*(4)
Special Issue

ISSN-e 2594-0317

34. Abitaev, K.; Qawasmi, Y.; Atanasova, P.; Dargel, C.; Bill, J.; Hellweg, T.; Sottmann, T. *Colloid Polym. Sci*. **2020**. *299*, 243-258. DOI:https://doi.org/10.1007/s00396-020-04791-5/Published.
35. Zhu, H.; Zhang, Y.; Zhu, J.; Li, Y.; Jiang, S.; Wu, N.; Wei, Y.; Zhou, J.; Song, Y. *J. Mater. Chem. A Mater*. **2020**, *8*, 22929-22937. DOI: https://doi.org/10.1039/d0ta06975b.
36. Gaulding, E. A.; Liu, G.; Chen, C. T.; Löbbert, L.; Li, A.; Segev, G.; Eichhorn, J.; Aloni, S.; Schwartzberg, A. M.; Sharp, I. D.; Toma, F. M. *J. Mater. Chem. A Mater.* **2017**, *5*, 11601-11614. DOI: https://doi.org/10.1039/c7ta00512a.
37. Qu, H. Y.; Wang, J.; Montero, J.; Li, Y.; Österlund, L.; Niklasson, G. A. *J. Appl. Phys.* **2021**, *129*, 1-11. DOI: https://doi.org/10.1063/5.0043673.
38. Kousik, S. R.; Sipp, D.; Abitaev, K.; Li, Y.; Sottmann, T.; Koynov, K.; Atanasova, P. *Nanomaterials*. **2021,** *11*, 196, 1-18. DOI: https://doi.org/10.3390/nano11010196.
39. Wang, T.; Yu, Q.; Zhang, S.; Kou, X.; Sun, P.; Lu, G. *Nanoscale.* **2018**, *10*, 4841–4851. DOI: https://doi.org/10.1039/c7nr08366a.
40. Li, Q.; Yang, C. *Mater Lett.* **2017**, *199*, 168–171. DOI: https://doi.org/10.1016/J.MATLET.2017.04.058.
41. Meng, S.; Li, D.; Wang, P.; Zheng, X.; Wang, J.; Chen, J.; Fang, J.; Fu, X. P *RSC Adv.* **2013**, *3*, 17021-17028. DOI: https://doi.org/10.1039/c3ra42618a.
42. Lin, X.; Chen, M. *Appl. Sci*. **2016**, *6*, 259, 1-10. DOI: https://doi.org/10.3390/app6100259.
43. Zhou, Q.; Pu, J.; Sun, X.; Zhu, C.; Li, J.; Wang, J.; Chang, S.; Zhang, H. I *J. Mater. Chem. A Mater.* [Online] **2017**, *5*, 14873–14880. DOI: https://doi.org/10.1039/c7ta03044d.
44. Tran, G. T. H.; Koike, M.; Uchikoshi, T.; Fudouzi, H. *Adv. Powder Technol.* **2020**, *31*, 3085–3092. DOI: https://doi.org/10.1016/J.APT.2020.05.029.
45. Rogach, A. L.; Kotov, N. A.; Koktysh, D. S.; Ostrander, J. W.; Ragoisha, G. A. *Chem. Mater.* **2000**, *12*, 2721-2726. DOI: https://doi.org/10.1021/cm000274l.
46. Galle, L.; Ehrling, S.; Lochmann, S.; Kaskel, S.; Bischoff, L.; Grothe, J. *ChemNanoMat.* **2020**, *6*, 560-566. DOI: https://doi.org/10.1002/cnma.201900731.
47. Li, Z. Y.; Zhang, Z. Q. *Phys. Rev. B Condens. Matter. Mater. Phys.* **2000**, *62*, 1516-1519. https://doi.org/10.1103/PhysRevB.62.1516.
48. Stöber, W.; Fink, A.; Bohn, *J. Colloid. Interface Sci.* **1968**, *26*, 62–69. DOI: https://doi.org/10.1016/0021-9797(68)90272-5.
49. Blanco, A.; Chomski, E.; Grabtchak, S.; Ibisate, M.; John, S.; Leonard, S. W.; Lopez, C.; Meseguer, F.; Miguez, H.; Mondla, J. P.; Ozin, G. A.; Toader, O.; Van Driel, H. M. *Nature.* **2000**, *405,* 437-440. DOI: https://doi.org/10.1038/35013024.
50. Salvarezza, R. C.; Vázquez, L.; Míguez, H.; Mayoral, R.; López, C.; Meseguer, F. *Phys. Rev. Lett.* **1996**, *77*, 4572-4575. DOI: https://doi.org/10.1103/PhysRevLett.77.4572.
51. Salinas, G.; Frontana-Uribe, B. A.; Reculusa, S.; Garrigue, P.; Kuhn, A. *Anal. Chem.* **2018**, *90*, 11770–11774. DOI: https://doi.org/10.1021/acs.analchem.8b03779.
52. Yi, D. K.; Lee, J. H.; Rogers, J. A.; Paik, U. *Appl. Phys. Lett.* **2009**, *94*. DOI: https://doi.org/10.1063/1.3089219.
53. Song, T.; Jeon, Y.; Samal, M.; Han, H.; Park, H.; Ha, J.; Yi, D. K.; Choi, J. M.; Chang, H.; Choi, Y. M.; Paik, U. *Energy Environ. Sci.* **2012**, *5*, 9028–9033. DOI: https://doi.org/10.1039/c2ee22358a.
54. Waleczek, M.; Dendooven, J.; Dyachenko, P.; Petrov, A. Y.; Eich, M.; Blick, R. H.; Detavernier, C.; Nielsch, K.; Furlan, K. P.; Zierold, R. *Nanomaterials*. **2021**, *11*, 1-16. DOI: https://doi.org/10.3390/nano11041053.
55. Kim, K. H.; Yoon, K. H.; Yun, J. H.; Ahn, B. T. *Electrochem. Solid-State Lett.* **2006**, *9*, A382-A385. DOI: https://doi.org/10.1149/1.2208011.

J. Mex. Chem. Soc. **2023**, *67*(4)
Special Issue

ISSN-e 2594-0317

56. Shin, S. S.; Kim, K.; Yoo, J.; Kim, J. H.; Ahn, S.; Cho, A.; Kim, D.; Jo, Y.; Jeong, I.; Shin, D.; Cho, J. S.; Yun, J. H.; Park, J.; Park, J. H. *Solar Energy Mater. Solar Cells.* **2021**, *224*, 1-11. DOI: https://doi.org/10.1016/J.SOLMAT.2021.111010.
57. Scharrer, M.; Wu, X.; Yamilov, A.; Cao, H.; Chang, R. P. H. *Appl. Phys. Lett.* **2005**, *86*, 151113. DOI: https://doi.org/10.1063/1.1900957.
58. Gong, X.; Lou, X.; Kim, S. B.; Gordon, R. G. *ACS Appl. Electron. Mater.* **2021**, *3*, 845-853. DOI: https://doi.org/10.1021/acsaelm.0c00977.
59. Mandati, S.; Sarada, B. V.; Dey, S. R.; Joshi, S. V. Pulsed Electrochemical Deposition of CuInSe2 and Cu(In,Ga)Se2 Semiconductor Thin Films. in: *Semiconductors - Growth and Characterization*; Inguanta R. and Sunseri C., Ed.; InTech: United Kingdom, **2018**; Chapter 6. DOI: https://doi.org/10.5772/intechopen.71857.
60. Sun, H.; Qin, D.; Huang, S.; Guo, X.; Li, D.; Luo, Y.; Meng, Q. *Energy Environ. Sci.* **2011**, *4*, 2630-2637. DOI:https://doi.org/10.1039/c0ee00791a (.
61. Park, J. Y.; Kim, S.; Hong, D. M.; Lim, J. W.; Yoo, C. J.; Dong, W. J.; Lee, J. L. *Electron. Mater. Lett.* **2019**, *15*, 454–461. DOI: https://doi.org/10.1007/s13391-019-00145-8.
62. Wang, J.; Zhou, H.; Nanda, J.; Braun, P. V. *Chem. Mater.* **2015**, *27*, 2803–2811. DOI: https://doi.org/10.1021/cm504365s.
63. Fei, J. Y.; Wilcox, G. D. *Electrochim. Acta.* **2005**, *50*, 2693–2698. DOI: https://doi.org/10.1016/j.electacta.2004.11.014.
64. Zhao, J.; Sun, L.; Canepa, S.; Sun, H.; Yesibolati, M. N.; Sherburne, M.; Xu, R.; Sritharan, T.; Loo, J. S. C.; Ager, J. W.; Barber, J.; Mølhave, K.; Xu, Z. J. *J. Mater. Chem. A Mater.* **2017**, *5*, 11905-11916. DOI: https://doi.org/10.1039/c7ta01871a.
65. Golden, T. D.; Shumsky, M. G.; Zhou, Y.; VanderWerf, R. A.; Van Leeuwen, R. A.; Switzer, J. A. *Chem. Mater*. **1996**, *8*, 2499-2509. DOI: https://doi.org/10.1021/cm9602095.
66. Zhang, Z.; Kitada, A.; Fukami, K.; Yao, Z.; Murase, K. *Electrochim. Acta*. **2020**, *348,* 136289-1-136289-10. DOI: https://doi.org/10.1016/j.electacta.2020.136289.
67. Pham, K.; Temerov, F.; Saarinen, J. J. *Mater. Des.* **2020**, *194*, 108886. DOI: https://doi.org/10.1016/J.MATDES.2020.108886.
68. Tello, A.; Boulett, A.; Sánchez, J.; Pizarro, G. del C.; Soto, C.; Linarez Pérez, O. E.; Sanhueza, R.; Oyarzún, D. P. *Chem. Phys. Lett.* **2021**, *778*, 138825. DOI: https://doi.org/10.1016/J.CPLETT.2021.138825.
69. Li, L.; Zhai, T.; Bando, Y.; Golberg, D. *Nano Energy*. **2011**, 91–106. DOI: https://doi.org/10.1016/j.nanoen.2011.10.005.
70. Zhang, C.; Shao, M.; Ning, F.; Xu, S.; Li, Z.; Wei, M.; Evans, D. G.; Duan, X. Au *Nano Energy*. **2015**, *12*, 231–239. DOI: https://doi.org/10.1016/J.NANOEN.2014.12.037.
71. Wolcott, A.; Smith, W. A.; Kuykendall, T. R.; Zhao, Y.; Zhang, J. Z. *Adv. Funct. Mater.* **2009**, *19*, 1849-1856. DOI:https://doi.org/10.1002/adfm.200801363.
72. Subalakshmi, K.; Senthilselvan, J.; Kumar, K. A.; Kumar, S. A.; Pandurangan, A. *J. Mater. Sci.: Mater. Electron.* **2017**, *28*, 15565–15595. DOI: https://doi.org/10.1007/s10854-017-7445-x.
73. (73) Tantray, A. M.; Shah, M. A. *Chem. Pap.* **2020**, *75*, 1739–1747. https://doi.org/10.1007/s11696-020-01419-4.
74. Lv, R.; Wang, T.; Su, F.; Zhang, P.; Li, C.; Gong, J. *Nano Energy*. **2014**, *7*, 143–150. DOI: https://doi.org/10.1016/J.NANOEN.2014.04.020.
75. Zhang, B.; Wang, F.; Zhu, C.; Li, Q.; Song, J.; Zheng, M.; Ma, L.; Shen, W. *Nano-Micro Lett*. **2016**, *8,* 137-142. DOI: https://doi.org/10.1007/s40820-015-0068-y.

76. Guo, J. H.; Vayssieres, L.; Persson, C.; Ahuja, R.; Johansson, B.; Nordgren, J. *J. Phys. Condens. Matter*. **2002**, *14,* 6969-6974. DOI: https://doi.org/10.1088/0953-8984/17/1/022.
77. Galsin, J. S. in: *Solid State Physics: An Introduction to Theory*; 1st ed.; Academic Press; United Kingdom, **2019**; 1. DOI: https://doi.org/10.1016/C2018-0-01175-5.
78. Shetty, A.; Nanda, K. K. *Appl. Phys. A Mater. Sci. Process.* **2012**, *109*, 151–157. DOI: https://doi.org/10.1007/s00339-012-7023-2.
79. Gilani, S.; Ghorbanpour, M.; Parchehbaf Jadid, A. *J. Nanostruct. Chem.* **2016**, *6*, 183–189. DOI: https://doi.org/10.1007/s40097-016-0194-1.
80. Basu, P. K.; Saha, N.; Maji, S.; Saha, H.; Basu, S. *J. Mater. Sci. Mater. Electron.* **2008**, *19*, 493–499. DOI: https://doi.org/10.1007/s10854-008-9604-6.
81. Mika, K.; Socha, R. P.; Nyga, P.; Wiercigroch, E.; Małek, K.; Jarosz, M.; Uchacz, T.; Sulka, G. D.; Zaraska, L. *Electrochim. Acta.* **2019**, *305*, 349–359. DOI: https://doi.org/10.1016/J.ELECTACTA.2019.03.052.
82. He, S.; Zheng, M.; Yao, L.; Yuan, X.; Li, M.; Ma, L.; Shen, W. P *Appl. Surf. Sci.* **2010**, *256*, 2557–2562. https://doi.org/10.1016/J.APSUSC.2009.10.104.
83. Kim, S. J.; Choi, J. *Electrochem. Commun.* **2007**, *10*, 175–179. DOI: https://doi.org/10.1016/j.elecom.2007.11.014.
84. Goh, H. S.; Adnan, R.; Farrukh, M. A. *Turk. J. Chem*. **2011**, *35*, 375–391. DOI: https://doi.org/10.3906/kim-1010-742.
85. Ramirez-Canon, A.; Miles, D. O.; Cameron, P. J.; Mattia, D. *RSC Adv*. **2013**, *3*, 25323-25330. DOI: https://doi.org/10.1039/c2ra43886d.
86. Farrukh, M. A.; Thong, C. K.; Adnan, R.; Kamarulzaman, M. A. *Russ. J. Phys. Chem. A*. **2012**, *86*, 2041–2048. DOI: https://doi.org/10.1134/S0036024412130171.
87. Zhao, J.; Wang, X.; Liu, J.; Meng, Y.; Xu, X.; Tang, C. *Mater. Chem. Phys.* **2011**, *126*, 555–559. DOI: https://doi.org/10.1016/j.matchemphys.2011.01.028.
88. Hu, Z.; Chen, Q.; Li, Z.; Yu, Y.; Peng, L. M. *J. Phys. Chem. C.* **2009**, *114*, 881–889. DOI: https://doi.org/10.1021/jp9094744.
89. Miles, D. O.; Cameron, P. J.; Mattia, D. *J. Mater. Chem. A Mater.* **2015**, *3*, 17569–17577. DOI: https://doi.org/10.1039/c5ta03578c.
90. Park, J.; Kim, K.; Choi, J. *Curr. Appl. Phys.* **2013**, *13*, 1370–1375. DOI: https://doi.org/10.1016/j.cap.2013.04.015.
91. Mateen Tantray, A.; Shah, M. A. *Chem. Phys. Lett.* **2020**, *747,* 137346. DOI: https://doi.org/10.1016/j.cplett.2020.137346.
92. Batista-Grau, P.; Sánchez-Tovar, R.; Fernández-Domene, R. M.; García-Antón, J. *Surf. Coat Technol.* **2019**, *381,* 125197. DOI: https://doi.org/10.1016/j.surfcoat.2019.125197.
93. Kim, S. J.; Lee, J.; Choi, J. *Electrochim. Acta.* **2008**, *53*, 7941–7945. DOI: https://doi.org/10.1016/j.electacta.2008.06.006.
94. Ilyas, U.; Rawat, R. S.; Tan, T. L.; Lee, P.; Chen, R.; Sun, H. D.; Fengji, L.; Zhang, S. *J. Appl. Phys.* **2011**, *110*, 093522. DOI: https://doi.org/10.1063/1.3660284.
95. Juárez, B. H.; García, P. D.; Golmayo, D.; Blanco, A.; López, C. *Adv. Mater.* **2005**, *17*, 2761–2765. DOI:https://doi.org/10.1002/adma.200500569.
96. Wang, B. S.; Li, R. Y.; Zhang, Z. Y.; Xing-Wang; Wu, X. L.; Cheng, G. A.; Zheng, R. T. *Catal Today.* **2019**, 321-322,100–106. DOI: https://doi.org/10.1016/j.cattod.2018.02.028.
97. Sayão, F. A.; Martins, A. S.; da Silva, J. J.; Boldrin Zanoni, M. V. *J. Electrochem. Soc.* **2021**, *168*, 076503. DOI: https://doi.org/10.1149/1945-7111/ac0ec5.

98. Muniyappa, M.; N. Kalegowda, S.; Shetty, M.; Sriramoju, J. B.; Shastri, M.; Navakoteswara, N. R.; De, D.; M.V., S.; Rangappa, D. *Int. J. Hydrogen Energy*. **2021**, *47*, 5307–5318. DOI: https://doi.org/10.1016/j.ijhydene.2021.11.171 (.
99. Goh, S. W.; Buckley, A. N.; Lamb, R. N.; Skinner, W. M.; Pring, A.; Wang, H.; Fan, L. J.; Jang, L. Y.; Lai, L. J.; Yang, Y. W. *Phys. Chem. Miner.* **2006**, *33*, 98–105. DOI: https://doi.org/10.1007/s00269-006-0058-1.
100. Shombe, G. B.; Khan, M. D.; Zequine, C.; Zhao, C.; Gupta, R. K.; Revaprasadu, N. *Sci. Rep.* **2020**, *10*, 3260. DOI: https://doi.org/10.1038/s41598-020-59714-9.
101. Youn, J.-S.; Jeong, S.; Oh, I.; Park, S.; Mai, H. D.; Jeon, K.-J. *Catalysts*. **2020**, 10, 1274. DOI: https://doi.org/10.3390/catal10111274.
102. Yang, X.; Zhou, L.; Feng, A.; Tang, H.; Zhang, H.; Ding, Z.; Ma, Y.; Wu, M.; Jin, S.; Li, G. *J. Mater. Res.* **2014**, *29*, 935–941. DOI: https://doi.org/10.1557/jmr.2014.74.
103. Dai, Z.; Xue, L.; Zhang, Z.; Gao, Y.; Wang, J.; Gao, Q.; Chen, D. *Energy Fuels.* **2020**, *34*, 10178–10187. DOI: https://doi.org/10.1021/acs.energyfuels.0c01797.
104. Shankar, A.; Elakkiya, R.; Maduraiveeran, G. *New J. Chem.* **2020**, *44*, 5071-5078. DOI: https://doi.org/10.1039/d0nj00192a.
105. Guan, B.; Li, Y.; Yin, B.; Liu, K.; Wang, D.; Zhang, H.; Cheng, C. *Chem. Eng. J.* **2016**, *308*, 1165–1173. DOI: https://doi.org/10.1016/j.cej.2016.10.016.
106. Li, H.; Wang, J.; Chu, Q.; Wang, Z.; Zhang, F.; Wang, S. *J. Power Sources.* **2009**, *190*, 578–586. DOI: https://doi.org/10.1016/j.jpowsour.2009.01.052.
107. Li, Y.; Ye, K.; Cheng, K.; Yin, J.; Cao, D.; Wang, G. *J .Power Sources.* **2014**, *274*, 943–950. DOI:https://doi.org/10.1016/j.jpowsour.2014.10.156.
108. Zhu, B. T.; Wang, Z.; Ding, S.; Chen, J. S.; Lou, X. W. *RSC Adv.* **2011**, *1*, 397–400. DOI: https://doi.org/10.1039/c1ra00240f.
109. Yu, L.; Yang, B.; Liu, Q.; Liu, J.; Wang, X.; Song, D.; Wang, J.; Jing, X. *J. Electroanal. Chem*. **2014**, *739*, 156–163. DOI: https://doi.org/10.1016/j.jelechem.2014.12.031.
110. Tang, S.; Vongehr, S.; Wang, Y.; Cui, J.; Wang, X.; Meng, X. *J. Mater. Chem. A Mater.* **2014**, *2*, 3648–3660. DOI: https://doi.org/10.1039/c3ta14541g.
111. Alegría, M.; Aliaga, Juan; Luis Ballesteros, Sotomayor-Torres, C.; González, G.; *Top Catal.* **2021**, *64*, 167–180. DOI: https://doi.org/10.1007/s11244-020-01360-6.
112. Panzeri, G.; Cristina, M.; Jagadeesh, M. S.; Bussetti, G.; Magagnin, L. *Sci. Rep*. **2020**, 10, 18730. DOI: https://doi.org/10.1038/s41598-020-75700-7.
113. Das, C.; Singh, A. K.; Heo, Y.; Aggarwal, G.; Maurya, S. K.; Seidel, J.; Kavaipatti, B. *J. Phys. Chem. C*. **2018**, *122*. DOI: https://doi.org/10.1021/acs.jpcc.7b10103.
114. Li, X.; Jiang, Y.; Shi, Z.; Xu, Z. *Chem. Mater.* **2007**, *19*, 5424-5430. DOI: https://doi.org/10.1021/cm071180f.
115. Chung, W. A.; Wu, C. J.; Hung, P. S.; Chou, S. C.; Guo, W. Q.; Wu, P. W. *J Taiwan Inst. Chem. Eng*. **2021**, *119*, 277–285. DOI: https://doi.org/10.1016/J.JTICE.2021.01.027.
116. Wan, C.; Jiao, Y.; Li, J. *J. Mater. Chem. A Mater.* **2017**, *5*, 17267-17278. DOI: https://doi.org/10.1039/c7ta04994c.
117. Chen, L.; Zhang, Y.; Zhu, P.; Zhou, F.; Zeng, W.; Daniel Lu, D.; Sun, R.; Wong, C. *Sci. Rep*. **2015**, *5*, 9672. DOI: https://doi.org/10.1038/srep09672.
118. Ahmad, W. R. W.; Mamat, M. H.; Khusaimi, Z.; Ismail, A. S.; Rusop, M. *Indonesian J. Electr. Eng. Comput. Sci.* **2018**, *13*, 1079–1086. DOI: https://doi.org/10.11591/ijeecs.v13.i3.pp1079-1086.

119. Shi, X.; Zhang, K.; Shin, K.; Moon, J. H.; Lee, T. W.; Park, J. H. *Phys. Chem. Chem. Phys.* **2013**, *15*. 11717-1722. DOI: https://doi.org/10.1039/c3cp50459j.

120. Mao, A.; Han, G. Y.; Park, J. H. *J. Mater. Chem.* **2010**, *20*, 2247–2250. DOI: https://doi.org/10.1039/B921965J.

121. Qiu, W. T.; Huang, Y. C.; Wang, Z. L.; Xiao, S.; Ji, H. B.; Tong, Y. X. *Wuli Huaxue Xuebao/ Acta Physico - Chimica Sinica*. Beijing University Press. **2017**, *33*, 80–102. DOI: https://doi.org/10.3866/PKU.WHXB201607293.

122. Ahn, H.-J.; Yoon, K.-Y.; Kwak, M.-J.; Jang, J.-H. *Angew. Chem., Int. Ed. Engl.* **2016**, *128*, 10076–10080. DOI: https://doi.org/10.1002/ange.201603666 (.

123. Shinde, P. S.; Annamalai, A.; Kim, J. Y.; Choi, S. H.; Lee, J. S.; Jang, J. S. Fine- *J. Phys. Chem. C.* **2015**, *119*, 5281–5292. DOI: https://doi.org/10.1021/jp5100186.

124. Smart, T. J.; Ping, Y. *J. Phys. Condens. Matter.* **2017**, *29*, 394006. DOI: https://doi.org/10.1088/1361-648X/aa7e3d.

125. Finger, L. W.; Hazen, R. M. *J. Appl. Phys.* **1980**, *51*, 5362–5367. DOI: https://doi.org/10.1063/1.327451.

126. Gilbert, B.; Frandsen, C.; Maxey, E. R.; Sherman, D. M. *Phys. Rev. B Condens. Matter. Mater. Phys.* **2009**, *79*, 035108. DOI: https://doi.org/10.1103/PhysRevB.79.035108.

127. Coey, J. M. D.; Sawatzkyt, G. A. *J. Phys. C. Solid State Phys*. **1971**, *4*, 2386-2407. DOI: https://doi.org/10.1088/0022-3719/4/15/025.

128. Cai, J.; Liu, H.; Liu, C.; Xie, Q.; Xu, L.; Li, H.; Wang, J.; Li, S. *Appl Surf Sci.* **2021**, *568,* 150606. DOI: https://doi.org/10.1016/j.apsusc.2021.150606.

129. Yi, S. S.; Wang, Z. Y.; Li, H. M.; Zafar, Z.; Zhang, Z. T.; Zhang, L. Y.; Chen, D. L.; Liu, Z. Y.; Yue, X. Z. *Appl. Catal. B.* **2021**, *283,* 119649. DOI: https://doi.org/10.1016/j.apcatb.2020.119649.

130. Tilley, S. D.; Cornuz, M.; Sivula, K.; Grätzel, M. *Angew. Chem., Int. Ed. Engl.* **2010**, *49*, 6405–6408. DOI: https://doi.org/10.1002/anie.201003110.

131. Mir, J. F.; Rubab, S.; Shah, M. A. *Chem. Phys. Lett.* **2020**, *741,* 137088. DOI: https://doi.org/10.1016/j.cplett.2020.137088.

132. Mohapatra, S. K.; John, S. E.; Banerjee, S.; Misra, M. *Chem. Mater.* **2009**, *21*, 3048–3055. DOI: https://doi.org/10.1021/cm8030208.

133. Sivula, K.; Zboril, R.; Le Formal, F.; Robert, R.; Weidenkaff, A.; Tucek, J.; Frydrych, J.; Grätzel, M. *J. Am. Chem. Soc.* **2010**, *132*, 7436–7444. DOI: https://doi.org/10.1021/ja101564f.

134. Maabong, K.; Machatine, A. G. J.; Mwankemwa, B. S.; Braun, A.; Bora, D. K.; Toth, R.; Diale, M. *Phys. B Condens. Matter.* **2018**, *535*, 67–71. DOI: https://doi.org/10.1016/j.physb.2017.06.054.

135. Yilmaz, C.; Unal, U. *RSC Adv.* **2015**, *5*, 16082–16088. DOI: https://doi.org/10.1039/c4ra16028b.

136. Shinde, P. S.; Go, G. H.; Lee, W. J. *J. Mater. Chem.* **2012**, *22*, 10469–10471. DOI: https://doi.org/10.1039/c2jm31254a.

137. Saremi-Yarahmadi, S.; Vaidhyanathan, B.; Wijayantha, K. G. U. *Int. J. Hydrogen Energy.* **2010**, *35*, 10155–10165. DOI: https://doi.org/10.1016/j.ijhydene.2010.08.004.

138. Phuan, Y. W.; Chong, M. N.; Zhu, T.; Yong, S. T.; Chan, E. S. *Mater. Res. Bull.* **2015**, *69*, 71–77. DOI: https://doi.org/10.1016/j.materresbull.2014.12.059.

139. Ling, Y.; Wang, G.; Wheeler, D. A.; Zhang, J. Z.; Li, Y. *Nano Lett.* **2011**, *11*, 2119–2125. DOI: https://doi.org/10.1021/nl200708y.

140. Roose, B.; Pathak, S.; Steiner, U. *Chem. Soc. Rev.* **2015**, 44, 8326-8349. DOI: https://doi.org/10.1039/c5cs00352k.

J. Mex. Chem. Soc. **2023**, *67*(4)
Special Issue
©2023, Sociedad Química de México
ISSN-e 2594-0317

141. Han, X.; Shao, G. *J. Phys. Chem. C.* **2011**, *115*, 8274-8282. DOI: https://doi.org/10.1021/jp1106586.
142. Yang, X.; Wu, X.; Li, J.; Liu, Y. TiO 2-Au *RSC Adv.* **2019**, *9*, 29097-29104. DOI: bhttps://doi.org/10.1039/c9ra05113a.
143. Yew, R.; Karuturi, S. K.; Liu, J.; Tan, H. H.; Wu, Y.; Jagadish, C. *Opt. Express.* **2019**, *27*, 761-773. DOI: https://doi.org/10.1364/oe.27.000761.
144. Spathis, P.; Karagiannidou, E.; Magoula-a3, A.-E. *Stud. Consev.* **2003**, *48*, 57–64. DOI: https://doi.org/10.1179/sic.2003.48.1.57.
145. Qian, Y.; Du, J.; Kang, D. J. *Microporous Mesoporous Mater.* **2019**, *273*, 148–155. DOI: https://doi.org/10.1016/J.MICROMESO.2018.06.056.
146. He, X.; Yang, C. P.; Zhang, G. L.; Shi, D. W.; Huang, Q. A.; Xiao, H. B.; Liu, Y.; Xiong, R. *Mater. Des.* **2016**, *106*, 74–80. DOI: https://doi.org/10.1016/J.MATDES.2016.05.025.
147. Ramadoss, A.; Kim, S. J. *J. Alloys Compd.* **2013**, *561*, 262–267. DOI: https://doi.org/10.1016/J.JALLCOM.2013.02.015.
148. Selvakumar, M.; Bhat, D. K. *Appl. Surf. Sci.* **2012**, *263*, 236–241. DOI: https://doi.org/10.1016/J.APSUSC.2012.09.036.
149. Hamed S. H. K. M. S. P. Thesis. Sudan University of Science & Technology (SUST), Faculty of Science-Department of Physics, Sep 2017. https://api.semanticscholar.org/CorpusID:55193279, accessed September 2019.
150. El-Kemary, M.; Nagy, N.; El-Mehasseb, I. *Mater. Sci. Semicond. Process.* **2013**, *16*, 1747–1752. DOI: https://doi.org/10.1016/J.MSSP.2013.05.018.
151. Koussi-Daoud, S.; Majerus, O.; Schaming, D.; Pauporté, T. *Electrochim. Acta.* **2016**, *219*, 638–646. DOI: https://doi.org/10.1016/j.electacta.2016.10.074.
152. Marrani, A. G.; Novelli, V.; Sheehan, S.; Dowling, D. P.; Dini, D. *ACS Appl. Mater. Interfaces.* **2014**, *6*, 143-152. DOI: https://doi.org/10.1021/am403671h.
153. Belousov, A. L.; Patrusheva, T. N.; Karacharov, A. A.; Ivanenko, A. A.; Kirik, S. D.; Khol'kin, A. I. *Theor. Found. Chem. Eng.* **2020**, *54*, 699–705. DOI: https://doi.org/10.1134/S0040579520040041.
154. Diao, C. C.; Huang, C. Y.; Yang, C. F.; Wu, C. C. *Nanomaterials.* **2020**, *10*, 636. DOI: https://doi.org/10.3390/nano10040636.
155. Ma, J.; Yang, J.; Jiao, L.; Mao, Y.; Wang, T.; Duan, X.; Lian, J.; Zheng, W. NiO *CrystEngComm.* **2012**, *14*, 453–459. DOI: https://doi.org/10.1039/c1ce05567d.
156. Tamirat, A. G.; Rick, J.; Dubale, A. A.; Su, W. N.; Hwang, B. J. *Nanoscale Horiz. Royal Soc. Chem.* **2016**, 243–267. DOI: https://doi.org/10.1039/c5nh00098j.
157. Beranek, R.; Kisch, H. *Electrochem. Commun.* **2007**, *9*, 761–766. DOI: https://doi.org/10.1016/j.elecom.2006.11.011.
158. Gai, Y.; Li, J.; Li, S. S.; Xia, J. B.; Wei, S. H. *Phys. Rev. Lett.* **2009**, *102*, 036402. DOI: https://doi.org/10.1103/PhysRevLett.102.036402.
159. Radecka, M.; Rekas, M.; Trenczek-Zajac, A.; Zakrzewska, K. *J. Power Sources.* **2008**, *181*, 46–55. DOI: https://doi.org/10.1016/j.jpowsour.2007.10.082.
160. Sasi, B.; Gopchandran, K. G. *Sol. Energy Mater. Sol. Cells.* **2007**, *91*, 1505–1509. DOI: https://doi.org/10.1016/j.solmat.2007.04.019.
161. Sahoo, P.; Sharma, A.; Padhan, S.; Thangavel, R. *Superlattices Microstruct.* **2021**, *159,* 107050. DOI: https://doi.org/10.1016/j.spmi.2021.107050.
162. Yoo, J.; Kwak, I. H.; Kwon, I. S.; Park, K.; Kim, D.; Lee, J. H.; Lim, S. A.; Cha, E. H.; Park, J. *J. Mater. Chem. C Mater.* **2020**, *8*, 3240–3247. DOI: https://doi.org/10.1039/c9tc05703j.

©2023, Sociedad Química de México
ISSN-e 2594-0317

163. Katsounaros, I.; Cherevko, S.; Zeradjanin, A. R.; Mayrhofer, K. J. J. *Angew. Chem., Int. Ed. Engl*. **2014,** *53*, 102–121. DOI: https://doi.org/10.1002/anie.201306588.

164. Krol, R. Van de; Grätzel, M. Electronic Materials: Science & Technology. In: *Photoelectrochemical Hydrogen Production*; New York: USA. **2012**.

165. Hellman, A.; Wang, B. *Inorganics*. **2017**, 5, 2-27. DOI: https://doi.org/10.3390/inorganics5020037.

166. Iandolo, B.; Wickman, B.; Zorić, I.; Hellman, A. *J. Mater. Chem. A Mater.* **2015**, *3*, 16896-16912. DOI: https://doi.org/10.1039/c5ta03362d.

167. Pan, J.; Fu, Y.; Xiao, G.; Niu, J.; Cao, J.; Wang, J.; Zheng, Y.; Li, C. *J. Environ. Chem. Eng.* **2022**, *10*, 108587. DOI: https://doi.org/10.1016/j.jece.2022.108587.

168. Ma, L.; Xu, J.; Liu, Z.; Liu, Y.; Liu, X.; Xu, S. *J. Mater. Sci.* **2022**, *57*, 6734–6748. DOI: https://doi.org/10.1007/s10853-022-07064-4.

169. Yoon, S.; Kim, M.; Kim, I. S.; Lim, J. H.; Yoo, B. *J. Mater. Chem. A Mater*. **2014**, *2*, 11621–11627. DOI: https://doi.org/10.1039/c4ta00616j.

170. Hsu, Y. K.; Yu, C. H.; Chen, Y. C.; Lin, Y. G. *Electrochim. Acta*. **2013**, *105*, 62–68. DOI: https://doi.org/10.1016/j.electacta.2013.05.003 .

171. Yang, Y.; Xu, D.; Wu, Q.; Diao, P. *Sci. Rep.* **2016**, *6,* 35158. DOI: https://doi.org/10.1038/srep35158.

172. Grez, P.; Henríquez, R.; Muñoz, E.; Rojas, C.; Moreno, S.; Sessarego, G.; Heyser, C.; Celedón, C.; Schrebler, R. *Int. J. Electrochem. Sci.* **2016**, *14*, 5646-5653. DOI: https://doi.org/10.20964/2019.06.03.

173. Nian, J. N.; Hu, C. C.; Teng, H. *Int. J. Hydrogen Energy*. **2008**, *33*, 2897–2903. DOI: https://doi.org/10.1016/j.ijhydene.2008.03.052.